Cell Reports

A Patient-Derived Cell Atlas Informs Precision Targeting of Glioblastoma

Graphical Abstract

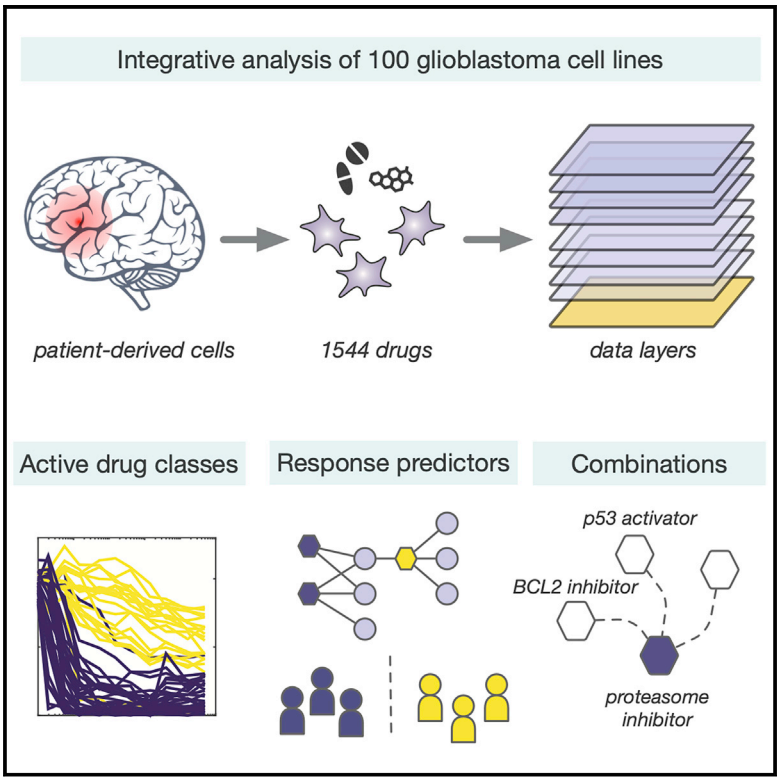

Authors

Patrik Johansson, Cecilia Krona, Soumi Kundu, ..., Marika Nestor, Silvia Marino, Sven Nelander

Correspondence

sven.nelander@igp.uu.se

In Brief

Johansson et al. report a systematic pharmacological and genomic characterization of a panel of 100 patient-derived glioblastoma cell cultures. An integrated analysis delineates subgroups with differential response to several drug classes and candidate targets, providing a resource to aid glioblastoma precision medicine.

Highlights

- A resource of 100 pharmacologically characterized patient-derived glioblastoma lines
- Integrated analyses define associations between drug response, pathways, and mutations
- The response to proteasome inhibitors is linked to *TP53* and *CDKN2A/B* aberrations

Johansson et al., 2020, Cell Reports *32*, 107897
July 14, 2020
https://doi.org/10.1016/j.celrep.2020.107897

Cell Reports

CellPress
OPEN ACCESS

Resource

A Patient-Derived Cell Atlas Informs Precision Targeting of Glioblastoma

Patrik Johansson,[1,8] Cecilia Krona,[1,8] Soumi Kundu,[1,8] Milena Doroszko,[1] Sathishkumar Baskaran,[1] Linnéa Schmidt,[1] Claire Vinel,[2] Elin Almstedt,[1] Ramy Elgendy,[1] Ludmila Elfineh,[1] Caroline Gallant,[1] Sara Lundsten,[1] Fernando J. Ferrer Gago,[3] Aleksi Hakkarainen,[4] Petra Sipilä,[4] Maria Häggblad,[5] Ulf Martens,[5] Bo Lundgren,[5] Melanie M. Frigault,[6] David P. Lane,[3,7] Fredrik J. Swartling,[1] Lene Uhrbom,[1] Marika Nestor,[1] Silvia Marino,[2] and Sven Nelander[1,9,*]

[1]Department of Immunology Genetics and Pathology, Science for Life Laboratory, Uppsala University, 751 85, Uppsala, Sweden
[2]Blizard Institute, Barts and The London School of Medicine and Dentistry, Queen Mary University of London, London E1 2AT, UK
[3]Laboratory, Agency for Science, Technology and Research (A*STAR), Singapore 138648, Singapore
[4]Institute of Biomedicine, Research Centre for Integrative Physiology and Pharmacology, University of Turku, 20500 Turku, Finland
[5]Department of Biochemistry and Biophysics, SciLifeLab, Stockholm University, 104 05 Stockholm, Sweden
[6]AstraZeneca Oncology, Waltham, MA 02451, USA
[7]Dept of Microbiology, Tumor and Cell Biology, Science for Life Laboratory, Karolinska Institutet, 17177 Stockholm, Sweden
[8]These authors contributed equally
[9]Lead Contact
*Correspondence: sven.nelander@igp.uu.se
https://doi.org/10.1016/j.celrep.2020.107897

SUMMARY

Glioblastoma (GBM) is a malignant brain tumor with few therapeutic options. The disease presents with a complex spectrum of genomic aberrations, but the pharmacological consequences of these aberrations are partly unknown. Here, we report an integrated pharmacogenomic analysis of 100 patient-derived GBM cell cultures from the human glioma cell culture (HGCC) cohort. Exploring 1,544 drugs, we find that GBM has two main pharmacological subgroups, marked by differential response to proteasome inhibitors and mutually exclusive aberrations in *TP53* and *CDKN2A/B*. We confirm this trend in cell and in xenotransplantation models, and identify both Bcl-2 family inhibitors and p53 activators as potentiators of proteasome inhibitors in GBM cells. We can further predict the responses of individual cell cultures to several existing drug classes, presenting opportunities for drug repurposing and design of stratified trials. Our functionally profiled biobank provides a valuable resource for the discovery of new treatments for GBM.

INTRODUCTION

The pharmacological treatment of glioblastoma (GBM) remains one of the hardest challenges in cancer precision therapy. An increasing volume of genetic data has clarified that GBM tumors present with multiple and diverse genetic aberrations in receptor tyrosine kinase (RTK), p53, and other pathways (Brennan et al., 2013; Taylor et al., 2019). Despite these advances, current therapy is based on a combination of surgery, radiation, and temozolomide, resulting in a median survival of 14.6 months, of which a mere 2.5 months are attributed to the chemotherapy (Stupp et al., 2005). Targeted intervention against key recurrent oncogenes in the RTK pathways, EGFR and PDGFRA, does not improve overall survival in unselected cohorts (Lee et al., 2015; Reardon et al., 2015; Brown et al., 2008). The impact of tumor diversity on GBM pharmacology thus remains to be elucidated.

To address this challenge, collections of patient-derived GBM cell cultures provide us with a powerful tool to explore and define possible pharmacological responses in GBM (Pollard et al., 2009; Xie et al., 2015). The analysis of drug response across a panel of GBM cell cultures can provide a relatively unbiased estimate of how drug responses vary, and their correlation (if any) with patient-specific factors, such as age, sex (Yang et al., 2019), frequent mutations, or transcriptional subtype (Verhaak et al., 2010; Wang et al., 2017). In a recent work, Lee et al. (2018) demonstrated that patient-derived GBM cells treated with drugs approved for oncology indications—predominantly kinase inhibitors—respond in a manner that can be predicted based on their somatic mutations. Traditional GBM cell lines, such as U87MG (Allen et al., 2016), have also been included in comparative pharmaco-genomic screens of tumor cell lines from diverse tissue origins (Kutalik et al., 2008; Barretina et al., 2012; Garnett et al., 2012; Yang et al., 2013; Basu et al., 2013; Seashore-Ludlow et al., 2015; Iorio et al., 2016). Despite these advances, the number of drug classes analyzed in well-characterized patient-derived GBM cell cultures remains limited, and there is scarce data to connect common drug classes to cellular pathways in GBM.

Here, we report a systematic effort to define the known and unknown pharmacological subclasses of GBM. Our strategy connects pharmacological and genomic profiling of 100 patient-derived GBM cell cultures, with computational modeling,

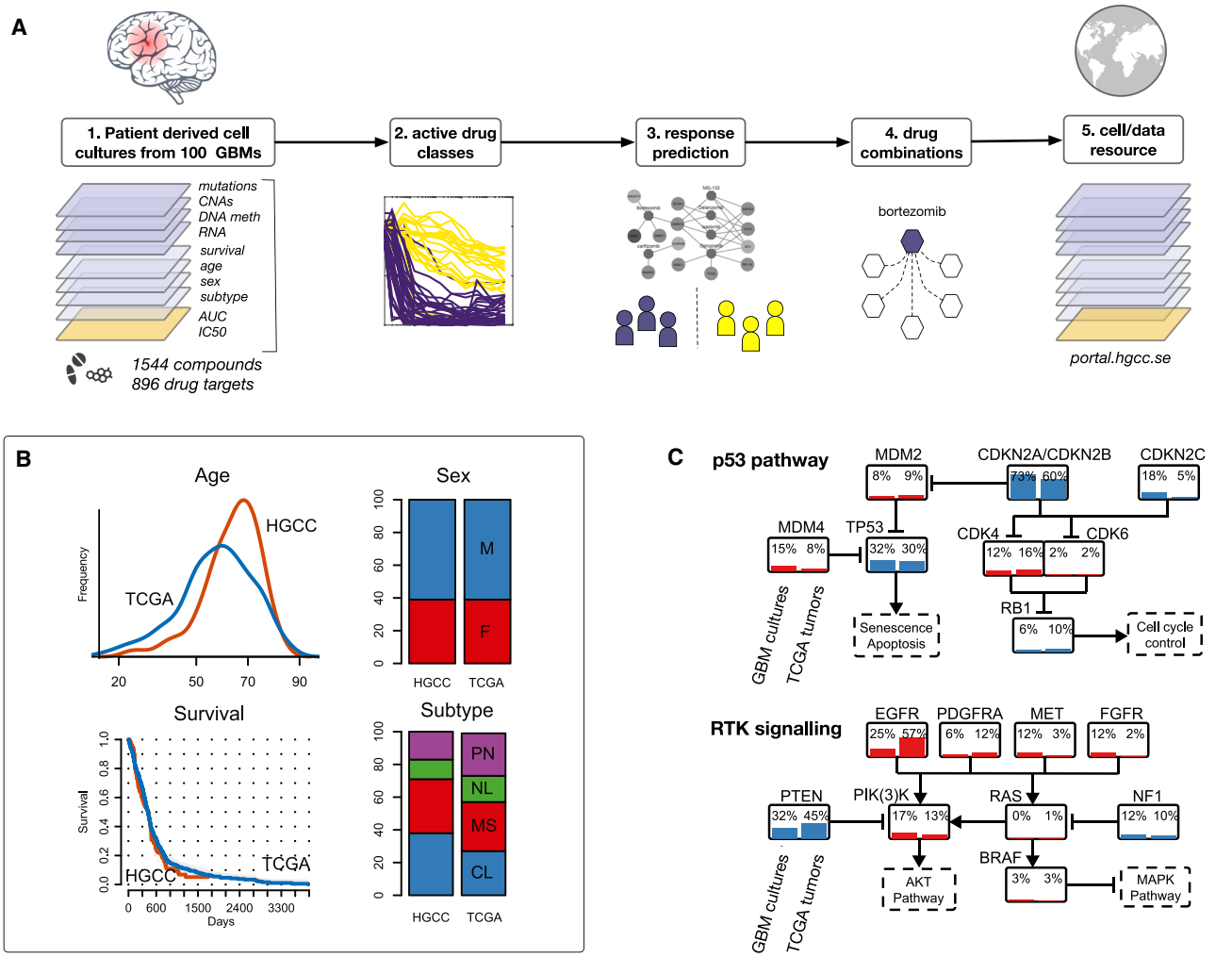

Figure 1. Study Overview and Genomic Characteristics of Primary GBM Cultures

(A) Study overview. Based on the integrated profiling of 100 patient-derived GBM cultures, we here develop network models of drug response, which identify p53 as a key determinant of pharmacological class.

(B) Cohort composition compared to the TCGA by age distribution, sex, survival, and transcriptional subtype.

(C) Alterations frequencies of key genes in the p53 and RTK/MAPK pathways, arranged as in Brennan et al. (2013). Note the similarity between primary GBM cultures and TCGA surgical samples across core GBM pathways (r = 0.82). Red, amplification or mutation; blue, deletion or mutation.

to identify (1) drugs and mechanisms of action (MOAs) with activity against primary GBM cells, (2) the key pathways associated to drug response, and (3) combinatorial interventions based on drug-pathway associations (Figure 1A). Previously, our laboratory has genetically characterized the human glioma cell culture (HGCC) resource of 48 public primary GBM lines, which has a broad distribution (Xie et al., 2015). The extended effort presented here aims to meet an unmet need for a large set of highly characterized cell models, with clinical annotations, comprehensive molecular information, as well as pharmacological and functional data.

From an unbiased survey of 1,544 compounds that comprise 116 MOAs, we identify a set of 248 drugs with GBM activity after 72 h of exposure. We use the variation in dose-dependent response to these drugs to define the main pharmacological classes of GBM and construct models that connect each individual drug (and drug class) to pathways and individual markers. The resulting map substantially extends the set of drug categories that can be predicted with accuracy in GBM, defines 51 associations between drug classes and hallmark pathways, and nominate biomarkers for drugs with both oncology and non-oncology indications. We find that GBM cultures exist in two main functional classes, not captured by current subtype systems. The classes are characterized by mutually exclusive p53 mutation and deletion of the *CDKN2A/B* locus, and differential sensitivity to proteasome inhibitors, a class of drugs that block the cellular catalysis of ubiquitinated proteins, leading to a surge of reactive oxygen species (ROS) and apoptotic cell death (Richardson et al., 2005; Ling et al., 2003; Lipchick et al., 2016). Exploiting additional compounds targeting pathways

CellPress
OPEN ACCESS

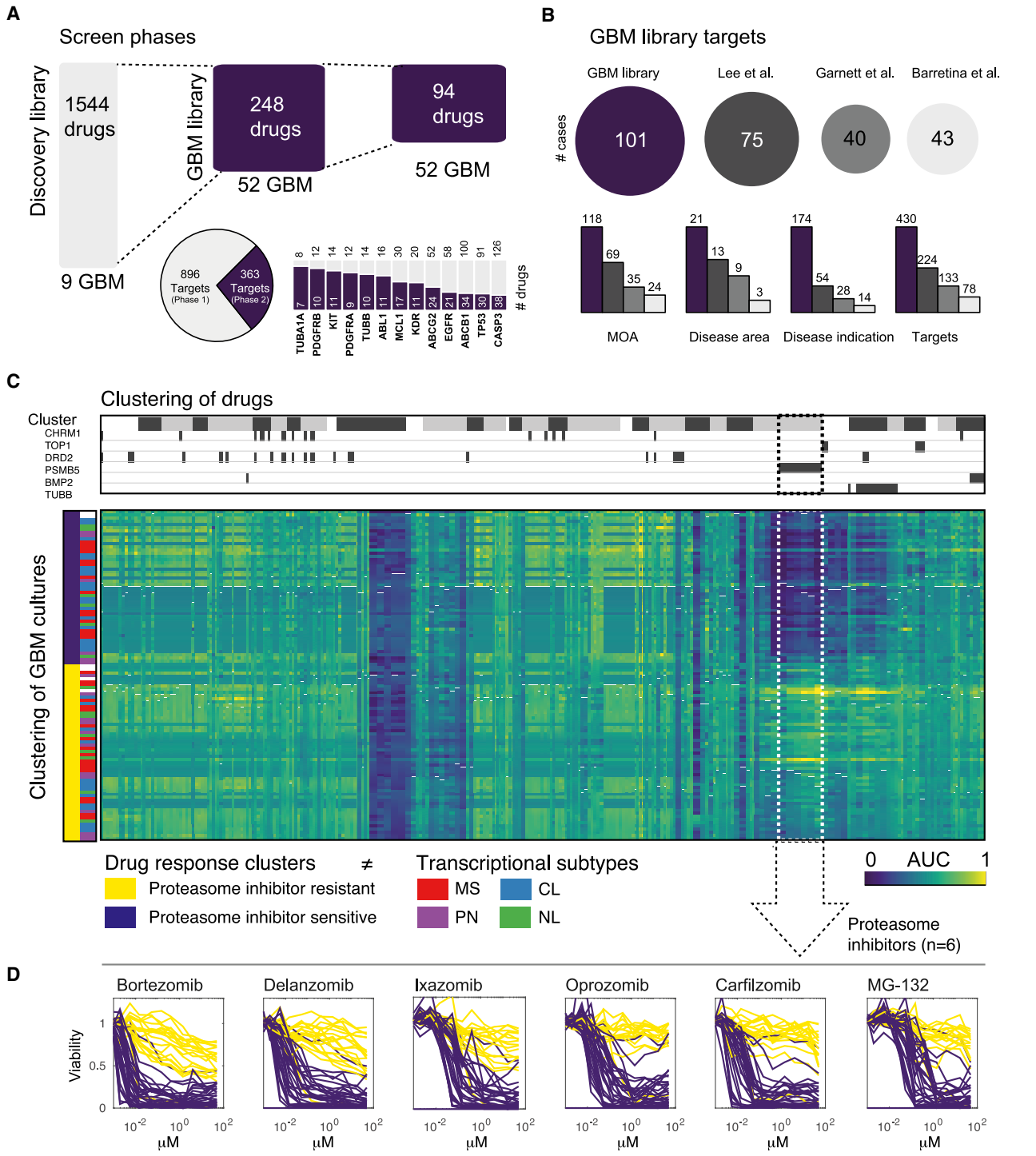

Figure 2. Defining the Global Variation of Drug Response in Primary GBM Cells

(A) Structure of the screen. A 1,544 drug discovery screen (phase 1) was followed by secondary and tertiary screens across, using focused libraries of drugs with GBM activity (phases 2 and 3). Drugs in our phase-2 library had 363 known targets, 75 of which were over-represented (empirical p value < 0.05) compared to the phase-1 library, e.g., EGFR, PDGFRA/B (indicated by bars).

(B) Drug target annotation of our GBM library, in comparison to recent studies of cancer cell panels. Mechanism of action (MOA), disease indication, and target from the Drug Repurposing Hub database.

(legend continued on next page)

linked to p53 and proteins encoded by the *CDKN2A/B* locus, we find that the resistance to proteasome inhibitors can be overcome by combinatorial targeting.

Our results demonstrate that an integrated study of primary GBM cells profiled at multiple levels can reveal unexpected associations between pathways and drug response, and underline the importance of the p53 and cyclin-dependent kinase (CDK) pathways in GBM precision therapy. The functionally characterized HGCC cell collection provides a resource for drug development, which we expect will enhance and expedite the development of new interventions against GBM.

RESULTS

Patient-Derived Cell Cultures Recapitulate the Known Molecular Heterogeneity of GBM

As our model for GBM drug response, we used 100 cultures from our HGCC collection at Uppsala University Hospital in Northern Europe, which underwent systematic genomic and pharmacological profiling (Figure 1A; Table S1). For these cultures to be a model of GBM diversity, they should recapitulate several layers of GBM heterogeneity, including molecular subtype, core pathway mutations, and chromosomal aberrations. We therefore established genomic background data for our cell cultures on several genomic platforms, which were compared to the corresponding molecular data from surgical GBM samples in The Cancer Genome Atlas (TCGA; Brennan et al., 2013). Our primary cultures corresponded well to TCGA in terms of patient age, survival times, patient sex, and molecular subtype (classical/proneural/mesenchymal system; Verhaak et al., 2010; Figure 1B). Our cultures also shared the spectrum of driver genes observed in TCGA at similar frequencies (Figure 1C, $R = 0.82$) and each culture retained genetic similarity to its source tumor (median of 27 mutations in common; 90% CI = 18.5–31.75; Figures S1A and S1B). We noted a slight reduction in the gene copy number of *EGFR* locus amplification (Figures S1C and S1D), which we interpret as loss of extrachromosomal *EGFR*-amplified genetic material unevenly distributed in mitosis as double minutes (Nikolaev et al., 2014). Still, the overall correlation of DNA copy number aberrations between our cell cultures and TCGA, however, was very high ($r^2 = 0.93$; Figures S1E and S1F). From this analysis, we conclude that our extended HGCC panel of primary cultures is genetically representative of GBM diversity as observed across patient tumors. Accordingly, pharmacological profiling of a large sample of diverse primary cells should reveal informative associations to drug response.

Sensitivity to Proteasome Inhibitors Defines Two Subclasses of GBM Cells

To explore the drug sensitivity of primary GBM cultures, we first implemented a discovery screen to select drugs for subsequent analysis across all 100 cultures. The discovery screen (Figure 2A, Phase 1) was carried out using a library of 1,544 annotated drugs, relevant for both oncology and other disease areas. Applying the library to nine GBM cultures of different subtypes, we identified the drugs that reduced viability in at least 3/9 cultures. These hits were compiled into a 248-drug library for profiling the GBM cultures in our collection. We carried out drug profiling in two phases, with 52 cell cultures each (Figure 2A, Phases 2 and 3). Drugs retained for phase 3 were the ones with the highest variability in viability response between cases. As determined by drug target databases (Drug Repurposing Hub and STITCH5), the library used had broad representation, covering 430 known drug targets, 118 MOA, and 21 disease areas (Figures 2A and 2B; Table S2). Among the 30 most active compounds, nine were previously unreported as candidates for GBM therapy (Table S2).

In each GBM culture, the effect of a drug was summarized as an area under the dose-response curve (AUC) score. Arranging these scores as a matrix of patient-derived cells (rows) and drugs (columns), we used hierarchical clustering to detect groups of cell cultures and drugs with strongly correlated behavior (Figure 2C). Notably, the best-fitted clustering robustly separated the cell cultures into two clusters, defined by sensitivity or resistance to a single class of drugs; proteasome inhibitors targeting PSMB5 and other proteasome units (Figure 2C). Graphing the dose-response curves for the six proteasome inhibitors in the data highlights the bimodal response to this category of drugs (Figure 2D). In our clustering of compounds, several drug targets other than the top hit PSMB5 ($p = 2.99 \times 10^{-9}$) were non-randomly distributed across clusters, such as the dopamine receptor (DRD2, $p = 5.71 \times 10^{-3}$), the muscarinic receptor (CHRM1, $p = 5.97 \times 10^{-4}$), spindle poisons (TUBB, $p < 1 \times 10^{-10}$), and BMP2 ($p = 2.52 \times 10^{-6}$; all p values corrected by Benjamini-Hochberg's (BH) method). Drugs targeting kinases EGFR and PDGFRA, which were strongly enriched as active against GBM cultures in the first screen ($p < 1 \times 10^{-5}$, BH-corrected, Figure 2A), did not exhibit such a significance, indicating that these are not the most promising candidates for therapy directed against specific GBM subgroups. Of note, we did not find a significant overlap between clusters of cell cultures and existing transcriptional subtypes. Also, unlike a recent report on sex differences in drug response (Yang et al., 2019), our data did not support that the drug sensitivities measured in our cohort were dependent on patient sex.

This analysis established that patient-derived GBM cells are primarily grouped by their sensitivity to proteasome inhibitors, and secondarily grouped by response to other classes of drugs. Since we found no evidence of an association between this grouping and obvious covariates such as GBM subtype or patient sex, we went on to investigate the data using an unbiased machine learning approach to identify associations between molecular data and drug response.

(C) Two-way clustering of primary GBM cultures (rows) and drugs (columns) based on area under the dose-response curve (AUC) scores. The GBM cultures were robustly grouped into two clusters that did not correlate with transcriptional subtype. The drugs were grouped into more than 10 clusters, many of which were enriched for drugs with a shared target (selected targets discussed in the text).
(D) The AUC of the six proteasome inhibitors in our library was bimodal (dashed box), and consistent across the inhibitors.

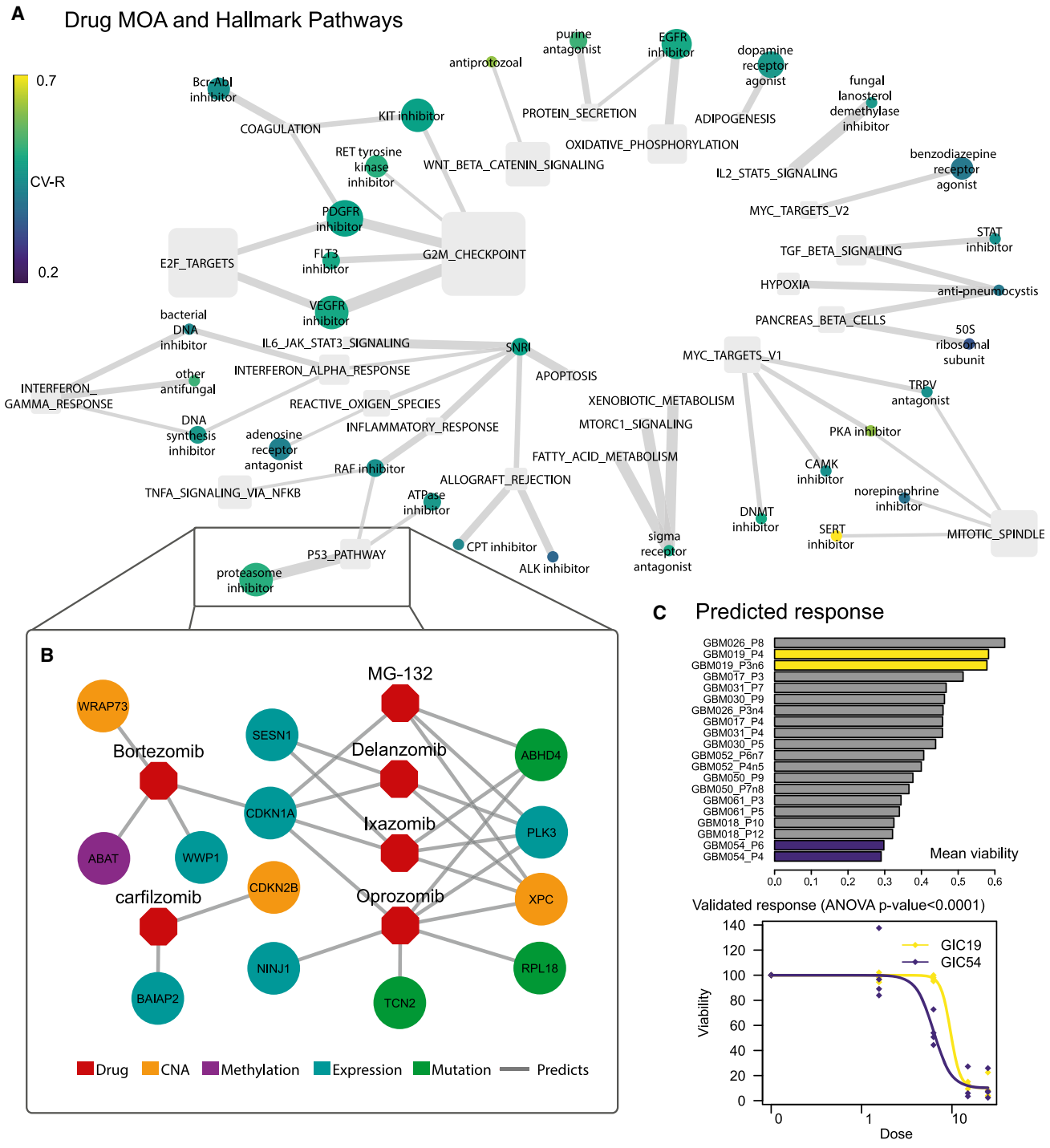

Figure 3. Network Analysis Links Proteasome Inhibitors to the p53 Pathway

(A) Drug response in primary GBM cultures correlates, in a drug-mechanism-dependent manner, with the transcriptional activity of specific pathways. The network describes statistically supported ($p < 0.05$) associations between drug MOA (green circles) and hallmark pathways in the molecular signature database (gray boxes). Nodes sizes are proportional to the number of involved drugs and genes, respectively, and line thickness is proportional to *–log*10 (p value) of the association. The MOA nodes are color-coded (dark green to yellow) based on their average predictive power (CV-R; c.f. Table S3).

(legend continued on next page)

Network Analysis Links Proteasome Inhibitors to the p53 Pathway

Integrating the collected data, we constructed statistical network models of drug responses in the GBM cells, with two specific goals in mind. First, we aimed to understand how activation of cellular pathways relates to drug response. Second, we aimed to define how well different classes of compounds can be predicted. To address the first problem, we computed the association between responses to individual drugs and 50 hallmark pathways, using Gene Set Enrichment Analysis (GSEA), retaining drug-pathway associations with q value < 0.1. We subsequently used information in the Drug Repurposing Hub database (Corsello et al., 2017) to group our compounds based on MOAs and used a Fisher test to find strong associations between pathways and MOAs. We summarized the result as a network in which links are pathway-to-MOA links with p value < 0.05 (Figure 3A). The network linked proteasome inhibitors to the expression of p53 hallmark genes, which was the most enriched hallmark pathway in this regard (p = 0.0043, Fisher's exact test with false discovery rate [FDR] correction). In total, 51 links were detected, containing both known relationships (e.g., between kinase inhibitors and cell cycle checkpoints) and interesting predictions (e.g., between sigma receptor inhibitors and lipid metabolism, Figure 3A).

Accurate Prediction of Drug Responses in Primary GBM Cells

In extended network analyses, we asked if additional layers of genomic data (e.g., mutations or DNA methylations) were associated with drug response and if the effect of different drugs could be predicted with accuracy, based on specific biomarkers. For this, we used a machine learning method, in which drug response (AUC) was the predicted variable, and other data were used as covariates. For an unbiased search, we let two well-defined algorithms (random forest and elastic net) select variables from RNA, copy number aberrations (CNA), and other data types to predict each individual drug. We used the leave-one-out cross-validation correlation (CV-R) as a metric of predictive power, which estimates the ability of the collected data to predict prospectively the variation in response in unseen cases on a scale from 0 (no predictive power) to 1.0 (perfect predictions). Other versions of cross validation, like leave-10-out, gave highly correlated results (Method Details). Previous versions of this approach have been successfully evaluated for cell cultures of mixed lineage origins (Kutalik et al., 2008; Barretina et al., 2012; Garnett et al., 2012; Yang et al., 2013; Basu et al., 2013; Seashore-Ludlow et al., 2015; Iorio et al., 2016). However, there is, so far, limited experience of the performance of machine learning in a well-characterized cohort of primary GBM lines.

In primary GBM cultures, a majority of drugs (262) could be predicted at a CV-R greater than 0.33, with remarkably high CV-R for particular drugs, such as clomipramine (CV-R = 0.76). Prediction power depended on the drug category. For instance, proteasome inhibitors had a higher average predictive power (CV-R = 0.44) than inhibitors of the tyrosine kinases EGFR, VEGFR, and PDGFR (CV-R 0.37 to 0.41; Table S3). The machine learning algorithm identified an association between several members of the p53 hallmark pathway (*CDKN1A*, *SESN1*) and the six different proteasome inhibitors (bortezomib, oprozomib, carfilzomib, MG-132, delanzomib, and ixazomib; Figure 3B). Consistent with the GSEA result, the number of network connections between proteasome inhibitors and p53 pathway genes was higher than expected by random, taking into account the size of the p53 pathway (Fisher's exact test, FDR-corrected p value = 0.0206). This suggests that a handful of markers in the p53 pathway can guide precision targeting using proteasome inhibitors. To further corroborate our cross-validation approach, we predicted the drug response in 10 cell cultures that were unseen by the algorithm, collected in a different hospital and profiled in a different center, and confirmed a differential response to bortezomib, measured by AUC (Figure 3C).

These analyses establish that drug responses of primary GBM cells can be associated to hallmark pathways and predicted with accuracy. The CV-R score of individual drugs (Table S2; Discussion) is an indication of that drug's potential for use in specific GBM subpopulations, and several drugs with high CV-R remain to be investigated as GBM therapies (Discussion). The best drug response predictions for primary GBM cells were often based on multiple markers, often from two or more types of genomic data (Figures S3A–S3C). Machine learning-based predictions were more accurate (higher CV-R on average) than corresponding predictions based on transcriptional subtype, clinical data, or mutation/expression of the drug target (Figures S3D and S3E).

An Axis of Mutually Exclusive *TP53* and *CDKN2A/B* Mutations in GBM

The association between drug response class and the p53 pathway motivated further analysis of genetic lesions in this pathway in our cell cultures. Gliomas are known to have different lesions affecting the p53 core pathway, ranging from mutations affecting p53 itself to indirect de-regulation via amplification of *MDM2*, or deletion of the *CDKN2A/B* locus (Figure 1C). The primary mechanism by which *CDKN2A/B* deletion affects p53 is through the loss of the CDKN2A gene product p14(ARF), a protein that blocks MDM2. Other gene products encoded by the *CDKN2A/B* locus are p16/INK4A and p15/INK4b, both of which block CDKs (Tao and Levine, 1999).

To visualize genetic variation in the p53 pathway we applied a principal component analysis. Sorting our HGCC lines (Figure 4A) and TCGA (Figure 4B) along the first component of variation placed each case along an axis, defined by gradual changes in p53 pathway gene expression and mutual exclusivity between p53 mutation and *CDKN2A/B* deletion (Fisher's test p = 0.0169 and p = 6.4401e-05; Figures 4A and 4B). The analysis thus

(B) Machine learning detects biomarkers of proteasome inhibitor response in GBM. The algorithm (bootstrap elastic net regression) detected a combination of mutations, CNAs, DNA methylation events, and transcripts as predictive. Selected transcripts were members of the p53 hallmark pathway.
(C) The machine learner predicted proteasome inhibitor response in GBM cells from unseen patients. Bar chart, the predicted viability in 20 primary GBM lines from a different hospital (Queen Mary, London). Cell cultures predicted to be sensitive (GBM54) and resistant (GBM19) were confirmed in a separate dose-response experiment (ANOVA p value = 0.0001, two cell cultures in four replicates each).

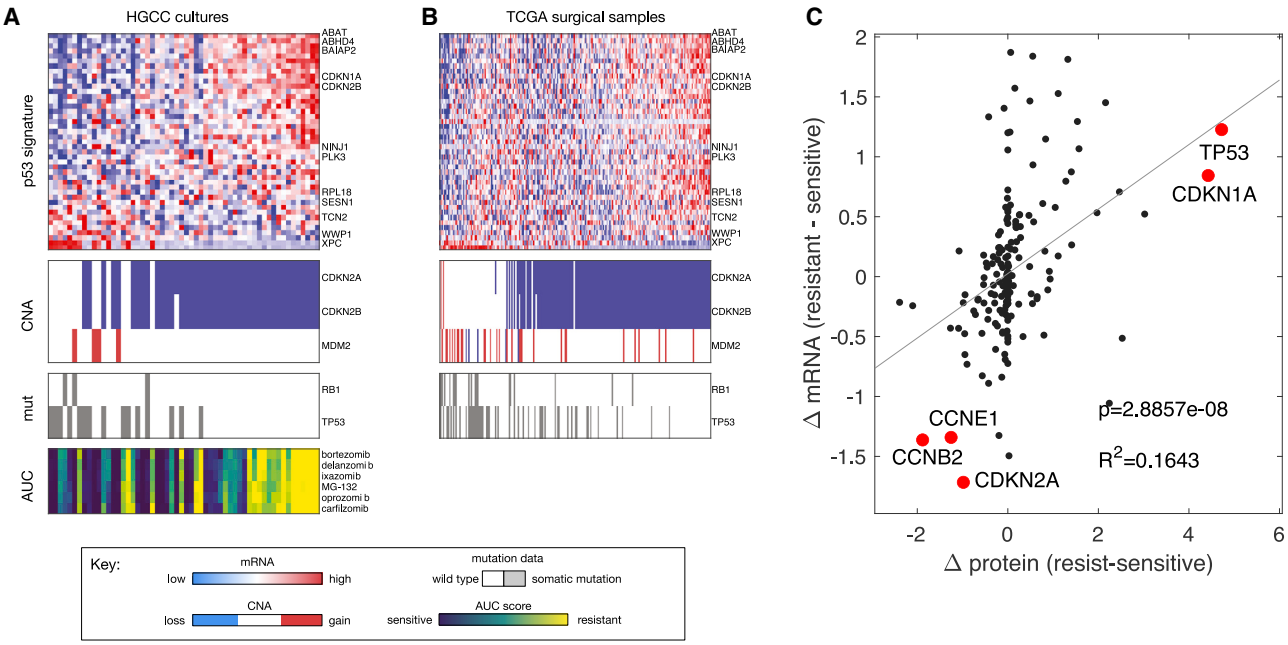

Figure 4. Aberrations of p53 and *CDKN2A/B* in Cell Cultures and Patient Samples

(A) HGCC cultures ordered according to the first principal component of the p53 pathway (Method Details). Note the mutual exclusion of p53 and *CDKN2A/B* aberrations.

(B) TCGA surgical samples ordered according to the corresponding first principal component.

(C) Differential expression of RNA (y axis) and protein (x axis) for 192 genes/proteins, comparing two sensitive versus two resistant lines.

clarified that transcripts selected by our network algorithm (Figure 3) are mostly expressed in *CDKN2A/B*-deleted cells with wild-type p53, and underlined that both cell cultures and surgical samples from gliomas can be categorized along a genetic and transcriptional axis, defined by mutually exclusive p53 and *CDKN2A/B* aberrations.

To explore if this distinction was also observed at the protein level, we measured a 192-protein profile in two p53 mutated and two *CDKN2A/B*-deleted cell cultures, by multiplexed proximity extension assays. We found a significant correlation between RNA and protein expression differences ($p < 10^{-7}$) and noted p53 itself and the direct p53 target *CDKN1A* (p21) as the main differentially expressed gene products (Figure 4C). Consistent with a loss of p15 and p16, the *CDKN2A/B* deleted cultures expressed higher levels of two cyclin proteins, indicating that these cell cultures also have a large population of cells with activated cyclin-CDK complexes committed to cell-cycle entry or mitosis (Figure 4C).

The *TP53-CDKN2A/B* Axis Orchestrates the Proteasome Inhibitor Response

Next, we asked how the observed variation in *TP53* and *CDKN2A/B* status correlates with the response to proteasome inhibitors in GBM cells. Based on the above analysis (Figure 4) we selected a set of 10 HGCC cultures, with representative variation in the p53 pathway signature, and with different mutation statuses of *TP53* and *CDKN2A/B* (Figure 5A). Among the 10, four were identified as *TP53* mutated by whole-exome and Sanger sequencing (Table S4), and three (U3054MG, U3173MG, and U3180MG) were unable to induce p21 protein, confirming the loss of p53 function (Figure S4B).

To get a global overview of how cellular pathways are impacted by proteasome inhibition, we first compared the transcriptional response following bortezomib treatment (10 nM, 6 h) in one sensitive (U3013MG) and one resistant (U3180MG) cell culture (Figure 5B). In both of the cell cultures, proteasome inhibition induced unfolded protein response (UPR), ROS, and p53 hallmark pathways in both lines and suppressed cell-cycle-promoting genes, but the resistant line showed a statistically stronger induction of genes involved in DNA damage response (DNA repair and ROS response) and in G2/M checkpoint regulators (Figure 5B). This suggested that resistant lines might differ in their ability to buffer ROS following proteasome inhibition, and in the activity of DNA repair pathways.

To explore these differences, we measured to what extent bortezomib induced the level of ROS in each of the cell cultures, as determined by the CM-H2DCFDA fluorometric assay as an indicator for ROS. Notably, the level of ROS induction was inversely proportional to the p53 signature (Figure 5C). The induction of ROS was also concomitant with elevated oxidized glutathione ratios (GSH/GSSG, Figure 5D), a tendency toward higher levels of Caspase-dependent apoptosis (Figure 5E), and accumulation of ubiquitinated protein in the sensitive lines (Figure S4C), suggesting ROS-mediated apoptosis as a key effector mechanism (c.f. Ling et al., 2003; Strauss et al., 2007). Consistent with this hypothesis, blocking ROS by anti-oxidants protected cells against bortezomib, and elevating ROS by proteotoxic stress using heat shock aggravated the response

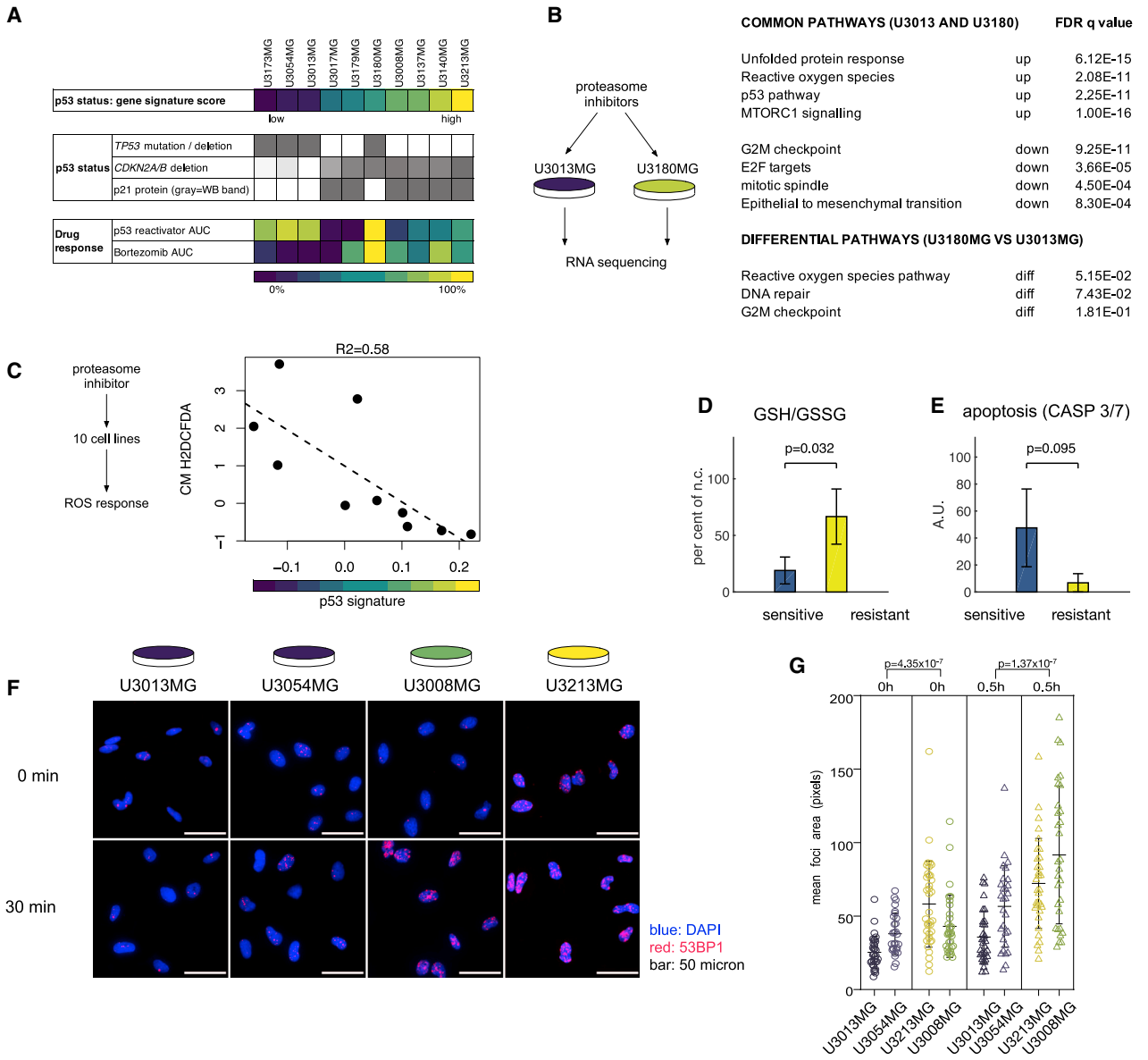

Figure 5. Cellular Effects of Bortezomib Treatment in a Panel of GBM Cells

(A) Sample of 10 GBM cell cultures for in-depth functional analysis. The p53 status gradient indicates the first principal component of the p53 signature. The gray boxes indicate the presence of p53 mutations, *CDKN2A/B* deletion, and p21 protein expression (see Figure S4A).

(B) RNA profiling comparison of one sensitive and one resistant line, measuring the log fold change of transcripts after 10-nM bortezomib for 6 h. Enrichment analysis of commonly affected (average fold change in both lines) pathways and differentially affected (fold-change difference) pathways. Fisher's test with FDR correction.

(C) p53 signature predicts ROS response. x axis, p53 signature principal component score as in Figure 4A; y axis, relative increase (a.u.) of ROS as measured by a fluorometric assay (linear regression, $R2 = 0.58$, $p = 0.0105$).

(D and E) Redox balance (D, GSH/GSSG ratio) and (E) apoptosis in bortezomib-resistant versus -sensitive patient-derived GBM cultures (n = 5 in each group, Wilcoxon rank sum test, bars are interquartile ranges).

(F) Comparison of induction of 53BP1 NHEJ DNA double-strand break processing and repair in four lines by bortezomib.

(G) Quantification of 53BP1 foci illustrated in (F). Student's t test; bars indicate standard deviation.

(Figure S4D). A number of p53-dependent ROS-suppressive genes were induced selectively in the resistant cells, as determined by quantitative PCR, including *SESN1* (Budanov, 2011), *NFE2L2* (Ahmad et al., 2016), and *TIGAR* (Bensaad et al., 2006), potentially explaining the effect (Figure S4A).

To assess differences in DNA repair, we stained two p53 mutant and two *CDKN2A/B*-deleted cultures for 53BP1 protein following bortezomib treatment (Figure 5F). We noted a significantly higher number of 53BP1 foci in resistant cell cultures, both at basal levels and following 30-min bortezomib

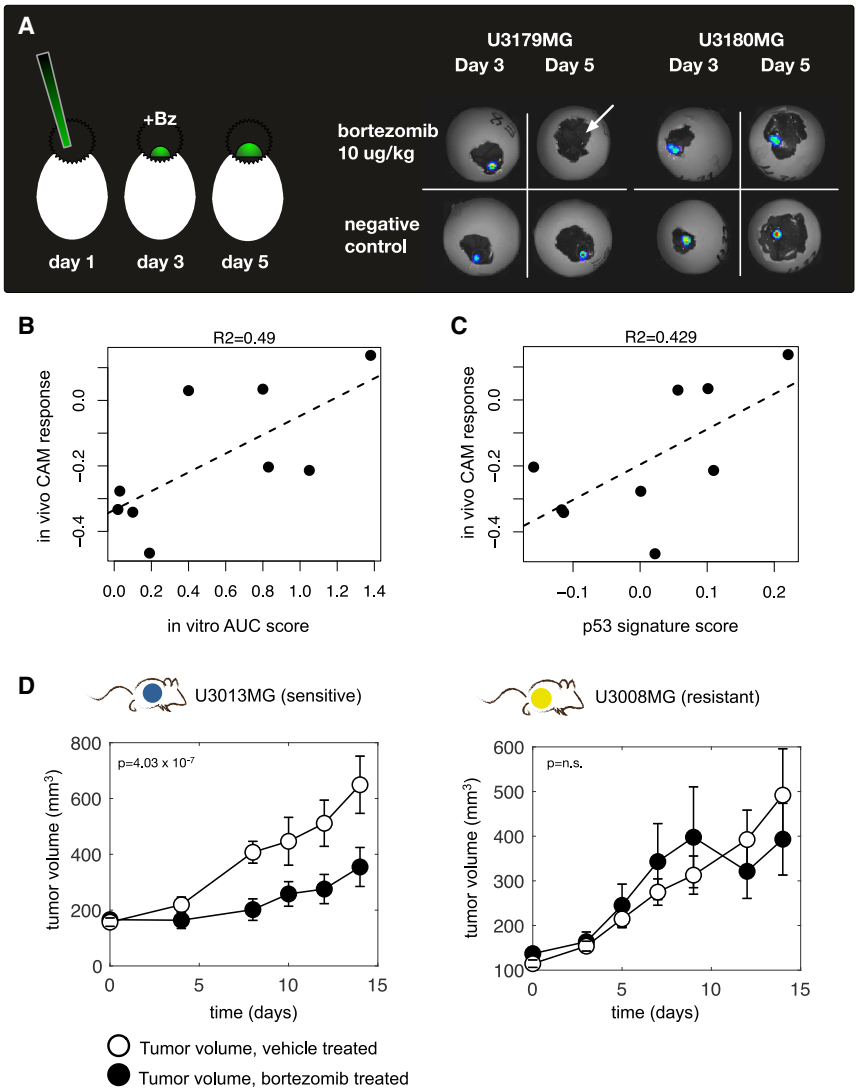

Figure 6. The *TP53/CDKNA2/B* Axis Determines *In Vivo* Responses and Predicts Tumor Growth

(A) The chorioallantoic membrane (CAM) *in vivo* assay was used to measure the response to bortezomib in nine patient-derived cell cultures.

(B) Correlation of CAM result and *in vitro* AUC viability score. x axis, average proteasome inhibitor AUC from the drug screen; y axis, negative values indicate a stronger response to bortezomib treatment.

(C) Correlation of CAM result (y axis) and p53 signature score (x axis, defined as in Figure 4A).

(D) Tumor growth rate of flank-xenografted-sensitive (U3013MG, CDKN2A wild-type [WT], p53 mutant [mut]) versus -resistant (U3008MG, CDKN2A del, p53 WT) GBM cells in immune-deficient mice, showing a selective bortezomib effect in tumors from sensitive cells. Bars are SEM and p values were obtained by a linear model comparing growth rates in bortezomib-treated versus mock (DMSO)-treated mice (seven mice per treatment).

treatment, indicating higher activity of the non-homologous end joining (NHEJ) DNA repair pathway (unpaired two-tailed t tests, $p < 0.0001$ both at basal level and after treatment; Figures 5F and 5G). Despite the induction of p21 protein in several of the cell cultures (Figure S4B), there were no signs of p21-induced G1 arrest. Rather, both the sensitive and resistant GBM lines respond to bortezomib treatment by G2/M arrest (Figure S5). The sensitive lines, however, reduced their S-phase population 2.9- to 3.1-fold following 10-nM bortezomib treatment compared to 1.3- to 1.8-fold in the resistant lines (Figure S5) alongside an increased proportion of cells in apoptosis (Figure 5E).

We conclude that in both p53 mutant and *CDKN2A/B*-deleted GBM cells, proteasome inhibition leads to G2/M arrest and ROS-dependent apoptosis. However, the quantitative balance between these outcomes is different; the more resistant cell cultures are less prone to apoptosis, and show signs of lower ROS induction and higher DNA repair activity.

The *TP53-CDKNA2/B* Axis Determines *In Vivo* Bortezomib Response

Next, we asked if the variation in p53 and *CDKN2A/B* aberrations would also inform the *in vivo* response to proteasome inhibition. To answer this, we evaluated nine of the above cell cultures in a transplantation-based model of drug response, the chicken chorioallantoic membrane (CAM) assay (DeBord et al., 2018). Using GFP-luciferase-tagged derivatives of each cell culture, we measured bioluminescence three days and five days post-inoculation onto the CAM (Figure 6A). When grown on the CAM, treatment by the proteasome inhibitor bortezomib reduced the growth of some, but not all the primary GBM cultures, at concentrations that were tolerated by the chick embryo (5–10 g/kg). The change in bioluminescence following proteasome inhibitor treatments agreed with the original drug-screen results for the nine cell cultures ($r = 0.73$, $p = 0.0189$; Figure 6B) and with the p53 gene signature score of the transplanted cell cultures ($r = 0.65$, $p = 0.0419$; Figure 6C). To explore these results in an independent model, we compared mice injected into the flank with a sensitive (U3013MG) and a resistant (U3008MG) cell culture. Significant reduction of tumor growth rate was seen only for the former ($p = 4.03 \times 10^{7}$, Figure 6D). These two experiments established that the variation observed in the initial drug screen was replicated *in vivo*.

Potentiating the Proteasome Inhibitor Responses in Glioma Cells

Our observation that a subset of cell cultures was less sensitive to proteasome inhibition motivated us to search for additional drugs that can be used to overcome proteasome inhibitor

resistance. Pharmacologically, such drugs should meet the criteria of synergism when combined with a proteasome inhibitor in GBM cells. To explore this possibility, we selected a set of 25 drugs in different categories (Figure 7A) including: (1) activators of p53, (2) apoptosis modulators, (3) kinase inhibitors against RTK and CDK pathways, (4) compounds that were statistically selected based on their anti-correlation with bortezomib, (5) compounds that target redox regulation, and (6) compounds that target genes that are selectively upregulated in resistant tumors.

We evaluated each of the 25 drugs using the combination index (CI), estimated from a response surface over a 6x6 matrix of doses, replicated in 4 to 10 cell cultures (Figure 7B). Next, we evaluated if the average CI was less than 1.0 across all cell cultures, thereby indicating that the compound consistently potentiates (i.e., is synergistic with) bortezomib (Figure 7C). As a second endpoint, we performed a regression test to evaluate if CI depends on the p53 signature (example in Figure 7D).

Thirteen of the tested compounds potentiated bortezomib in multiple cell cultures (Figure 7E). Strong overall synergism was obtained with two p53 activators, the peptide-based MDM2 blocker PM2 (Spiegelberg et al., 2018) and the small molecule MDM2 blocker AMG232. By contrast, the mutant p53 selective reactivator PRIMA-1 showed selective single-agent activity in p53 mutant cells but did not potentiate bortezomib (Figure 7E, right column). Notably, all three apoptosis modulators potentiated bortezomib, as did the CDK2 inhibitor milciclib. This indicated that higher levels of wild-type p53 protein or a lowered apoptotic threshold both suffice to potentiate bortezomib in primary GBM cells. For seven of the 13 potentiating compounds, a wild-type p53 signature was associated with a lower CI value, indicating stronger synergism (Figure 7E). This shows that bortezomib can be potentiated especially in the more resistant type of cells with wild-type p53 and *CDKN2A/B* deletion. One exception to this trend was mTOR inhibitor torin-2, which selectively potentiated bortezomib in p53 mutant cells, which may indicate a differential dependency on this pathway as indicated by our RNA profiling results (c.f. Figure 5B).

Interestingly, the three compounds selected in a purely data-driven fashion, by virtue of anti-correlation to bortezomib in Phase-2 and -3 screening data (the calcium channel blocker cilnidipine, the microtubule depolymerizing drug nocodazole, and the antibiotic spectinomycin), were all synergistic (Figure 7E, group iv). More studies would be required to elucidate the mechanism, but we speculate that a common denominator among all three might be the induction of unfolded protein stress. As an independent test of the synergies, we evaluated two of the selected combinations in a 3D sphere culture system (Figure 7F) and noted significantly lower viability in spheres treated by bortezomib and navitoclax or milciclib (Figure 7G).

In contrast to the consistent synergism for these drug classes, we found limited evidence that co-targeting redox pathways would potentiate bortezomib, e.g., the NRF2-targeted agent costunolide (Ahmad et al., 2016; not shown).

We conclude that both Bcl-2 family inhibitors and p53 activators show promise as potentiators of proteasome inhibitors in GBM cells. Because the potentiating effect is stronger in *CDKN2A/B* deleted (often more bortezomib resistant) cell cultures, the results suggest a strategy to also target these cells. We also find signs that automatically nominated compounds, selected by virtue of their anti-correlation in the screening data, make good combination partners.

DISCUSSION

The goal of our study was to identify new opportunities for GBM precision medicine, by an integrated study of patient-derived GBM cells. Previously, an initial set of 48 glioma cell cultures has been distributed as the HGCC resource (Xie et al., 2015). By extending this collection to 100 cell cultures, and by characterizing the cells at multiple genomic and functional levels, we detected associations between hallmark pathways and multiple drug classes, thus providing a starting point for research investigating drug repurposing and precision therapy.

As a validation of our resource, we investigate the detected association between the p53 pathway and the sensitivity to several proteasome inhibitors. The impact of mutations in the tumor suppressor p53 and *CDKN2A/B* loci on the efficacy of proteasome inhibitors remains to be fully understood. On the one hand, p53 is identified as one major mechanism underlying the effect of proteasome inhibitors because proteasome inhibition can induce apoptosis through stabilization of p53 protein (Xue et al., 2019). On the other hand, proteasome inhibitors can also be highly effective against p53 mutant cell lines of various tissue origins, such as glioma (Seol, 2011), epithelial carcinomas (Dabiri et al., 2017; Adams et al., 1999; Yerlikaya et al., 2015; Qiang et al., 2017), and blood malignancies (Strauss et al., 2007; Hideshima et al., 2001). Suggested mechanisms for this include p53-independent induction of p73 (Dabiri et al., 2017), and induction of apoptosis-regulating proteins such as DR5 (TRAILR2; Qiang et al., 2017; Yerlikaya et al., 2015). Of the 10 cell cultures that we investigated in detail, seven had signs of functional p53, indicated by their ability to induce p21 after genotoxic stress. Less is known about how *CDKN2A/B* deletion affects proteasome inhibitor response, but since it is established that proteins encoded by the locus (e.g., p16/INK4A) are modulated by the proteasome pathway, such effects are plausible. Taking these factors into account, the model we propose for the relative resistance to proteasome inhibitors in some GBM cell cultures is that the level of p53 activation stays under a threshold, insufficient to induce apoptosis. This could be dependent on the increased synthesis of anti-oxidants, e.g., glutathione (Figure 5D), which scavenge ROS and more active DNA-damage-repair mechanisms in the proteasome inhibitor-resistant cell cultures (Figures 5F and 5G). Consistent with the proposed model, MDM2 inhibitors PM2 and AMG232 potentiated the bortezomib response and synergistically killed GBM cells, and all three agents that modulate the apoptotic threshold, such as navitoclax, potentiated bortezomib. Our results are thus consistent with a role for p53 in the response to proteasome inhibitors, in line with Yoo et al. (2017), Asklund et al. (2012), and Forte et al. (2019), but imply substantial quantitative and phenotypic differences in the response to proteasome inhibition. Further work, including quantitative mathematical modeling, will be needed to elucidate these differences and to chart the relative contributions of aberrations in p53 and *CDKN2A/B*, respectively.

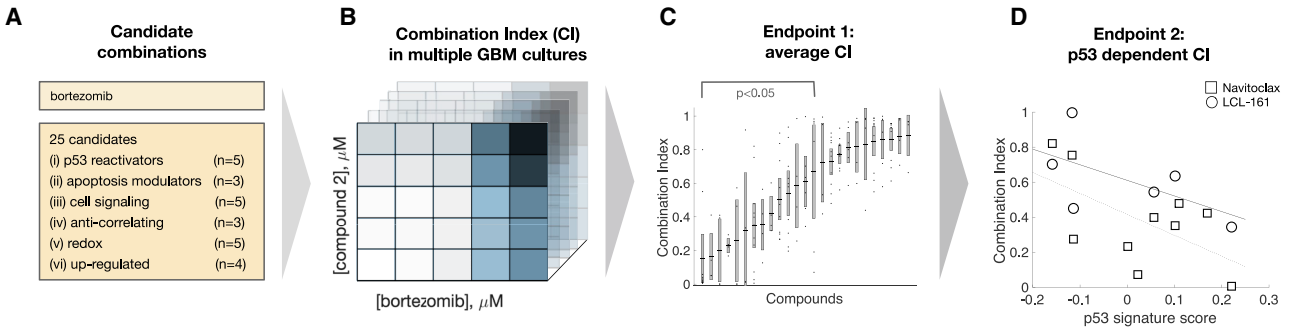

E

	Drug		AUC < 1	CI < 1		p53 dependent CI
(i)	MDM2/TP53	PM2	p=0	0.17±0.37	p=0	
	MDM2/TP53	AMG232	p=0.01	0.67±0.39	p=0.08	↘ p=0
	MDM2/TP53	VIP116	p=0	0.72±0.37	n.s.	
	TP53	PRIMA1	n.s	0.81±0.39	n.s.	
	MDM2/TP53	nutlin-3	n.s	0.86±0.39	n.s.	↘ p=0.036
(ii)	BCL2	navitoclax	p=0.05	0.42±0.37	p=0	↘ p=0.0086
	BCL2L1	WEHI-539	p=0	0.59±0.41	p=0.03	
	BIRC2, XIAP	LCL-161	p=0.03	0.61±0.39	p=0.03	↘ p=0.081
(iii)	CDK2	milciclib	p=0.09	0.51±0.37	p=0	
	MTOR	torin-2	p=0	0.17±0.41	p=0	↗ p=0.028
	EGFR	gefitinib	p=0	0.53±0.37	p=0	
	ERK	XMD8-96	n.s	0.35±0.41	p=0	
	MET	volitinib	n.s	0.85±0.41	n.s.	
(iv)	CACNA1B	cilnidipine	n.s.	0.18±0.41	p=0	
	-	nocodazole	p=0	0.23±0.41	p=0	
	-	spectinomycin	no	0.35±0.41	p=0	↘ p=0.049
(v)	-	pterostilbene	n.s	0.3±0.41	p=0	↘ p=0.0045
	GSTA2	chloroquine	p=0	0.41±0.41	p=0	
	-	costunolide	p=0	0.85±0.37	*n.s.*	
	-	niclosamide	p=0	0.77±0.37	*n.s.*	
	ATP6V1A	bafilomycin A1	n.s	0±19.35	*n.s.*	
(vi)	CDK9	alvocidib	p=0	0.86±0.37	*n.s.*	
	KMO	Ro61-8048	n.s	0.76±0.41	*n.s.*	↘ p=0.0043
	PAK	FRAX486	p=0	0.89±0.41	*n.s.*	
	UGCG	DL-PDMP	n.s	0.84±0.41	*n.s.*	

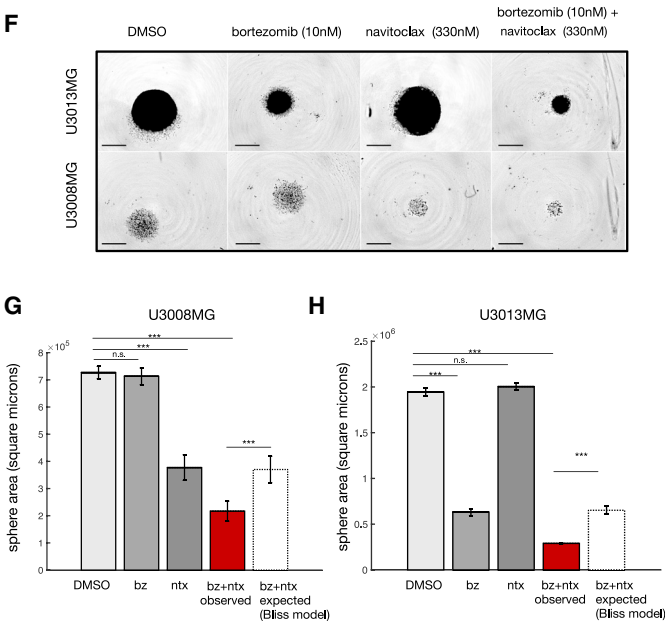

Figure 7. Modulation of Proteasome Inhibitor Response of Glioma Cells

(A) Based on our integrated data, we tested 25 compounds in combination with a proteasome inhibitor.

(B) Each compound was evaluated across a 6x6 dose-dose-response surface, replicated in multiple cell cultures with different p53 signature scores.

(C) Combination index (CI) statistics for 25 compounds, measured in 4 to 10 cell cultures per compound. x axis, compounds; y axis, CI values. Points are individual patient-derived cell cultures, boxes are 90% confidence intervals.

(D) Test for CI (y axis) dependency on p53 signature (x axis), for GBM cell cultures treated with navitoclax-bortezomib (squares) and LCL-161-bortezomib (circles)

(E) Summary; results for endpoint 1 (average CI < 1.0) and endpoint 2 (CI depends on p53 signature) are shaded based on p value. Arrows indicate a positive (up) or a negative (down, as in C) dependency on the p53 signature. The p values were obtained using Student's t tests (endpoint 1) and linear regression (endpoint 2), based on 4 to 10 cell cultures per combination.

(F) Sphere model to evaluate bortezomib in combination with navitoclax in one bortezomib-sensitive (U3013MG) and one resistant line (U3008MG). Bars, 800 m.

(G and H) Sphere size is significantly affected by bortezomib (G) and navitoclax (H) treatment. Red bar, observed sphere size after combination treatment. Dashed bar, expected sphere size after combination treatment, based on the Bliss model. Bars indicate 90% bootstrap confidence intervals of the mean (two biological replicates, each with seven technical replicates).

The clinical potential of the reported gene signature and combinations remains to be assessed. Among the publicly disclosed proteasome inhibitors, salinosporamide A (marizomib) shows promise for CNS tumors, as it penetrates the blood-brain barrier in rodent models (Di et al., 2016) and is under phase-3 investigation in humans (NCT03345095). Our proposed classification of glioma cells based on p53 and *CDKN2A/B* status has potential applications in the prospective design and *post hoc* interpretation of proteasome inhibitor clinical trials in GBM. Notably, germline mutation of both p53 (Li-Fraumeni syndrome) and *CDKN2A* (melanoma-astrocytoma syndrome) are associated with substantial risk increase for brain tumors. We speculate that the small group of patients with a GBM associated with Li Fraumeni syndrome might be a particularly interesting group for proteasome inhibitor treatment. The identified combinations provide a framework to study the potentiation of proteasome inhibitors. While many of the detected effects are robust across cells from multiple patients (particularly for Bcl-2 family inhibitors), more analysis is warranted to assess the efficacy and safety of such combinations.

In addition to the specific observations related to proteasome inhibitors, our analysis gives interesting general insights regarding GBM precision therapy. First, we note that the established subtypes (proneural, classical, and mesenchymal) are relatively weak predictors of drug response, compared to the optimally selected transcriptional or genetic markers. Also, the best performing biomarkers are not necessarily somatic point mutations, motivating the use of multiple data layers as a strategy to identify biomarkers for drug response in GBM cells (Figure S3). Second, the range of drugs whose response can be predicted with accuracy in primary GBM cells is broader than frequently investigated kinase inhibitors (c.f. Table S3). Drugs with high predictive performance (high CV-R) and strong effect (low AUC) in a subset of cell cultures are of particular interest for drug repurposing. Key examples of such drugs in our atlas include calcium modulators (digoxin, calcimycin [A23187], and niguldipine), three likely anti-metabolites (lycorine, thioguanosine, and perhexiline), an anti-malarial (quinacrine), modulators of dopaminergic transmission (sertindole and 5-nonloxytryptamin), antiseptics (hexetidine, chlorhexidine, and ciclopirox), and a cyclical peptide (thiostreptone), all with high ranking CV-R scores (Table S2). Accordingly, we propose that the proteins and pathways targeted by these drugs may warrant further investigation as candidates for stratified therapy of GBM. For instance, quinacrine (CV-R 0.54) is a known inhibitor of phospholipase A2 (PLA2), an enzyme that hydrolyzes phospholipids into second messengers that regulate cell proliferation, cell migration, and cell survival through binding of G-protein-coupled receptors (Moolenaar et al., 2004). High expression of PLA2 has been associated with poor prognosis and therapy resistance in glioma patients (Wu et al., 2019; Yang and Zhang, 2018). As a second example, the activity of digoxin and digitoxigenin may imply Na^{+}-K+ ATPase (ATP1A1) as a possible target in GBM, or other targets affected by digoxin drugs in GBM cells, such as HIF1alpha and HIF2alpha (Joseph et al., 2015). Last, we note that more than 80% of the GBM cultures are sensitive to omacetaxine mepesuccinate (homoharringtonine, CV 0.46), a blocker of the large 60S ribosomal subunit peptidyltransferase center (Garreau de Loubresse et al., 2014), with RPL3 as the possible target (Fresno et al., 1977; Tujebajeva et al., 1989), as well as the ribosomal inhibitor anisomycin (CV-R 0.45) further underlining ribosomal function or biogenesis as a possible target in a subset of GBM. Altogether, further experimental validation of compounds with high CV-R scores, in suitable cell-based and animal models, will be necessary to evaluate their potential for GBM precision therapy.

The presented extension of the HGCC biobank presents a valuable resource for GBM precision medicine, distributed as an open-access GBM cell culture library (hgcc.se) with associated databases (portal.hgcc.se) and networks of biomarker-drug associations, which can be analyzed in Cytoscape (Shannon et al., 2003) or compatible programs. Users are invited to explore the data and retrieve individual primary GBM cell cultures with known genomic parameters or drug sensitivity, for functional studies, or for data-driven modeling. Building on early successes with heterogeneous traditional cell lines (Kutalik et al., 2008; Barretina et al., 2012; Garnett et al., 2012; Yang et al., 2013; Basu et al., 2013; Seashore-Ludlow et al., 2015; Iorio et al., 2016), we expect that an increasing number of well-characterized and diagnosis-specific datasets will gradually increase both the predictive power, interpretability, and clinical relevance of cell culture panels.

STAR★METHODS

Detailed methods are provided in the online version of this paper and include the following:

- KEY RESOURCES TABLE
- RESOURCE AVAILABILITY
  - Lead Contact
  - Materials Availability
  - Data and Code Availability
- EXPERIMENTAL MODEL AND SUBJECT DETAILS
  - Cell culture collection methods
- METHOD DETAILS
  - Genomic profiling of patient-derived GBM cultures
  - Pharmacological profiling of patient-derived GBM cultures
  - Gene signature of p53 activity in GBM, and analysis of p53 status in 10 GBM cultures
  - RNA profiling and GSEA
  - Responses to proteasome inhibition in 10 GBM cultures with different p53 status
  - Details of proximity extension assay analysis
  - p53 targets and ROS levels in proteasome inhibitor-treated GBM cultures
  - Glutathione ratio and caspase 3/7 assays
  - Chicken chorioallantoic membrane assay
  - Mouse xenotransplantation and bortezomib treatment
  - Modulation of proteasome inhibitor responses by heat, antioxidants and potentiating drugs
  - Sphere growth combination treatments
  - BrdU cell cycle flow cytometric analysis of bortezomib treated GBM cultures
- QUANTIFICATION AND STATISTICAL ANALYSIS
  - Algorithms for glioblastoma subtype assignment
  - Drug target annotation
  - Algorithms for drug activity similarity and cluster analysis
  - Algorithms for construction of biomarker-drug network: drug response prediction based on multi-omic data
  - Algorithms for scoring drug synergism

SUPPLEMENTAL INFORMATION

Supplemental Information can be found online at https://doi.org/10.1016/j.celrep.2020.107897.

ACKNOWLEDGMENTS

We thank fellow investigators in HGCC, including the labs of Karin Forsberg Nilsson and Bengt Westermark. We thank the Array and Analysis Facility, Uppsala University, the team at the SciLifeLab Drug Discovery and Development (DDD) platform, and the Turku Center for Disease Modelling (TCDM), University of Turku, Finland. Support for this study was provided by the AstraZeneca-SciLifeLab Research Collaboration, the Swedish Research

Council, the Swedish Cancer Society, and the Swedish Childhood Cancer Foundation. Work in the Marino lab was supported by grants from Brain Tumour Research (Centre of Excellence Award) and Barts Charity (Barts Brain Tumour Centre).

AUTHOR CONTRIBUTIONS

The study was conceived by S.N. and coordinated by C.K.; the multi-omic profiling was performed by S.B. and L.E. and analyzed by P.J. and S.N.; the drug screen was performed by S.B., L.S., L.E., M.H., U.M., and B.L.; the integrative analysis was performed by P.J. and S.N.; the experiments in Figures 4, 5, and 7 were designed and performed by S.K., C.K., E.A., S.B., L.S., L.E., C.G., M.M.F., and R.E.; additional biobank characterization was performed by L.U. and F.J.S.; the CAM and mouse experiments in Figure 6 were designed by M.D., A.H., and P.S. and performed by C.K. and S.K.; C.V. and S.M. performed the prospective tests of proteasome inhibitor sensitivity; S.L., M.N., and D.P.L. contributed the analysis of p53-independent apoptosis and p53 activators; and the manuscript was written by S.N., P.J., and C.K., and finalized with contributions from all authors.

DECLARATION OF INTERESTS

The authors declare no competing interests.

Received: June 30, 2019
Revised: March 13, 2020
Accepted: June 22, 2020
Published: July 14, 2020

REFERENCES

Adams, J., Palombella, V.J., Sausville, E.A., Johnson, J., Destree, A., Lazarus, D.D., Maas, J., Pien, C.S., Prakash, S., and Elliott, P.J. (1999). Proteasome inhibitors: a novel class of potent and effective antitumor agents. Cancer Res. *59*, 2615–2622.

Ahmad, F., Dixit, D., Sharma, V., Kumar, A., Joshi, S.D., Sarkar, C., and Sen, E. (2016). Nrf2-driven TERT regulates pentose phosphate pathway in glioblastoma. Cell Death Dis. *7*, e2213.

Allen, M., Bjerke, M., Edlund, H., Nelander, S., and Westermark, B. (2016). Origin of the U87MG glioma cell line: good news and bad news. Sci. Transl. Med. *8*, 354re3.

Almstedt, E., Elgendy, R., Hekmati, N., Rosén, E., Wärn, C., Olsen, T.K., Dyberg, C., Doroszko, M., Larsson, I., Sundström, A., et al. (2020). Integrative discovery of treatments for high-risk neuroblastoma. Nat. Commun. *11*, 71.

Asklund, T., Kvarnbrink, S., Holmlund, C., Wibom, C., Bergenheim, T., Henriksson, R., and Hedman, H. (2012). Synergistic killing of glioblastoma stem-like cells by bortezomib and HDAC inhibitors. Anticancer Res. *32*, 2407–2413.

Barbie, D.A., Tamayo, P., Boehm, J.S., Kim, S.Y., Moody, S.E., Dunn, I.F., Schinzel, A.C., Sandy, P., Meylan, E., Scholl, C., et al. (2009). Systematic RNA interference reveals that oncogenic KRAS-driven cancers require TBK1. Nature *462*, 108–112.

Barretina, J., Caponigro, G., Stransky, N., Venkatesan, K., Margolin, A.A., Kim, S., Wilson, C.J., Lehár, J., Kryukov, G.V., Sonkin, D., et al. (2012). The Cancer Cell Line Encyclopedia enables predictive modelling of anticancer drug sensitivity. Nature *483*, 603–607.

Basu, A., Bodycombe, N.E., Cheah, J.H., Price, E.V., Liu, K., Schaefer, G.I., Ebright, R.Y., Stewart, M.L., Ito, D., Wang, S., et al. (2013). An interactive resource to identify cancer genetic and lineage dependencies targeted by small molecules. Cell *154*, 1151–1161.

Bensaad, K., Tsuruta, A., Selak, M.A., Vidal, M.N., Nakano, K., Bartrons, R., Gottlieb, E., and Vousden, K.H. (2006). TIGAR, a p53-inducible regulator of glycolysis and apoptosis. Cell *126*, 107–120.

Breiman, L. (2001). Random forests. Mach. Learn. *45*, 5–32.

Brennan, C.W., Verhaak, R.G., McKenna, A., Campos, B., Noushmehr, H., Salama, S.R., Zheng, S., Chakravarty, D., Sanborn, J.Z., Berman, S.H., et al.; TCGA Research Network (2013). The somatic genomic landscape of glioblastoma. Cell *155*, 462–477.

Brown, P.D., Krishnan, S., Sarkaria, J.N., Wu, W., Jaeckle, K.A., Uhm, J.H., Geoffroy, F.J., Arusell, R., Kitange, G., Jenkins, R.B., et al.; North Central Cancer Treatment Group Study N0177 (2008). Phase I/II trial of erlotinib and temozolomide with radiation therapy in the treatment of newly diagnosed glioblastoma multiforme: North Central Cancer Treatment Group Study N0177. J. Clin. Oncol. *26*, 5603–5609.

Budanov, A.V. (2011). Stress-responsive sestrins link p53 with redox regulation and mammalian target of rapamycin signaling. Antioxid. Redox Signal. *15*, 1679–1690.

Cibulskis, K., Lawrence, M.S., Carter, S.L., Sivachenko, A., Jaffe, D., Sougnez, C., Gabriel, S., Meyerson, M., Lander, E.S., and Getz, G. (2013). Sensitive detection of somatic point mutations in impure and heterogeneous cancer samples. Nat. Biotechnol. *31*, 213–219.

Corsello, S.M., Bittker, J.A., Liu, Z., Gould, J., McCarren, P., Hirschman, J.E., Johnston, S.E., Vrcic, A., Wong, B., Khan, M., et al. (2017). The Drug Repurposing Hub: a next-generation drug library and information resource. Nat. Med. *23*, 405–408.

Dabiri, Y., Kalman, S., Gürth, C.M., Kim, J.Y., Mayer, V., and Cheng, X. (2017). The essential role of TAp73 in bortezomib-induced apoptosis in p53-deficient colorectal cancer cells. Sci. Rep. *7*, 5423.

DeBord, L.C., Pathak, R.R., Villaneuva, M., Liu, H.C., Harrington, D.A., Yu, W., Lewis, M.T., and Sikora, A.G. (2018). The chick chorioallantoic membrane (CAM) as a versatile patient-derived xenograft (PDX) platform for precision medicine and preclinical research. Am. J. Cancer Res. *8*, 1642–1660.

Di, K., Lloyd, G.K., Abraham, V., MacLaren, A., Burrows, F.J., Desjardins, A., Trikha, M., and Bota, D.A. (2016). Marizomib activity as a single agent in malignant gliomas: ability to cross the blood-brain barrier. Neuro-oncol. *18*, 840–848.

Eisenberg, E., and Levanon, E.Y. (2003). Human housekeeping genes are compact. Trends Genet. *19*, 362–365.

Forte, I.M., Indovina, P., Iannuzzi, C.A., Cirillo, D., Di Marzo, D., Barone, D., Capone, F., Pentimalli, F., and Giordano, A. (2019). Targeted therapy based on p53 reactivation reduces both glioblastoma cell growth and resistance to temozolomide. Int. J. Oncol. *54*, 2189–2199.

Fresno, M., Jiménez, A., and Vázquez, D. (1977). Inhibition of translation in eukaryotic systems by harringtonine. Eur. J. Biochem. *72*, 323–330.

Gagnon-Bartsch, J.A., and Speed, T.P. (2012). Using control genes to correct for unwanted variation in microarray data. Biostatistics *13*, 539–552.

Garnett, M.J., Edelman, E.J., Heidorn, S.J., Greenman, C.D., Dastur, A., Lau, K.W., Greninger, P., Thompson, I.R., Luo, X., Soares, J., et al. (2012). Systematic identification of genomic markers of drug sensitivity in cancer cells. Nature *483*, 570–575.

Garreau de Loubresse, N., Prokhorova, I., Holtkamp, W., Rodnina, M.V., Yusupova, G., and Yusupov, M. (2014). Structural basis for the inhibition of the eukaryotic ribosome. Nature *513*, 517–522.

1000 Genomes Project Consortium; Auton, A., Brooks, L.D., Durbin, R.M., Garrison, E.P., Kang, H.M., Korbel, J.O., Marchini, J.L., McCarthy, S., McVean, G.A., and Abecasis, G.R. (2015). A global reference for human genetic variation. Nature *526*, 68–74.

Guintivano, J., Aryee, M.J., and Kaminsky, Z.A. (2013). A cell epigenotype specific model for the correction of brain cellular heterogeneity bias and its application to age, brain region and major depression. Epigenetics *8*, 290–302.

Hellemans, J., Mortier, G., De Paepe, A., Speleman, F., and Vandesompele, J. (2007). qBase relative quantification framework and software for management and automated analysis of real-time quantitative PCR data. Genome Biol. *8*, R19.

Hideshima, T., Richardson, P., Chauhan, D., Palombella, V.J., Elliott, P.J., Adams, J., and Anderson, K.C. (2001). The proteasome inhibitor PS-341 inhibits growth, induces apoptosis, and overcomes drug resistance in human multiple myeloma cells. Cancer Res. *61*, 3071–3076.

Hoshida, Y. (2010). Nearest template prediction: a single-sample-based flexible class prediction with confidence assessment. PLoS ONE *5*, e15543.

Iorio, F., Knijnenburg, T.A., Vis, D.J., Bignell, G.R., Menden, M.P., Schubert, M., Aben, N., Gonçalves, E., Barthorpe, S., Lightfoot, H., et al. (2016). A landscape of pharmacogenomic interactions in cancer. Cell *166*, 740–754.

Jin, C., Fotaki, G., Ramachandran, M., Nilsson, B., Essand, M., and Yu, D. (2016). Safe engineering of CAR T cells for adoptive cell therapy of cancer using long-term episomal gene transfer. EMBO Mol Med *8*, 702–711.

Joseph, J.V., Conroy, S., Pavlov, K., Sontakke, P., Tomar, T., Eggens-Meijer, E., Balasubramaniyan, V., Wagemakers, M., den Dunnen, W.F., and Kruyt, F.A. (2015). Hypoxia enhances migration and invasion in glioblastoma by promoting a mesenchymal shift mediated by the HIF1α-ZEB1 axis. Cancer Lett. *359*, 107–116.

Koboldt, D.C., Zhang, Q., Larson, D.E., Shen, D., McLellan, M.D., Lin, L., Miller, C.A., Mardis, E.R., Ding, L., and Wilson, R.K. (2012). VarScan 2: somatic mutation and copy number alteration discovery in cancer by exome sequencing. Genome Res. *22*, 568–576.

Kutalik, Z., Beckmann, J.S., and Bergmann, S. (2008). A modular approach for integrative analysis of large-scale gene-expression and drug-response data. Nat. Biotechnol. *26*, 531–539.

Langfelder, P., Zhang, B., and Horvath, S. (2008). Defining clusters from a hierarchical cluster tree: the Dynamic Tree Cut package for R. Bioinformatics *24*, 719–720.

Larson, D.E., Harris, C.C., Chen, K., Koboldt, D.C., Abbott, T.E., Dooling, D.J., Ley, T.J., Mardis, E.R., Wilson, R.K., and Ding, L. (2012). SomaticSniper: identification of somatic point mutations in whole genome sequencing data. Bioinformatics *28*, 311–317.

Lee, E.Q., Kaley, T.J., Duda, D.G., Schiff, D., Lassman, A.B., Wong, E.T., Mikkelsen, T., Purow, B.W., Muzikansky, A., Ancukiewicz, M., et al. (2015). A multicenter, phase II, randomized, noncomparative clinical trial of radiation and temozolomide with or without vandetanib in newly diagnosed glioblastoma patients. Clin. Cancer Res. *21*, 3610–3618.

Lee, J.K., Liu, Z., Sa, J.K., Shin, S., Wang, J., Bordyuh, M., Cho, H.J., Elliott, O., Chu, T., Choi, S.W., et al. (2018). Pharmacogenomic landscape of patient-derived tumor cells informs precision oncology therapy. Nat. Genet. *50*, 1399–1411.

Liberzon, A., Birger, C., Thorvaldsdóttir, H., Ghandi, M., Mesirov, J.P., and Tamayo, P. (2015). The Molecular Signatures Database (MSigDB) hallmark gene set collection. Cell Syst. *1*, 417–425.

Ling, Y.H., Liebes, L., Zou, Y., and Perez-Soler, R. (2003). Reactive oxygen species generation and mitochondrial dysfunction in the apoptotic response to Bortezomib, a novel proteasome inhibitor, in human H460 non-small cell lung cancer cells. J. Biol. Chem. *278*, 33714–33723.

Lipchick, B.C., Fink, E.E., and Nikiforov, M.A. (2016). Oxidative stress and proteasome inhibitors in multiple myeloma. Pharmacol. Res. *105*, 210–215.

Mayrhofer, M., DiLorenzo, S., and Isaksson, A. (2013). Patchwork: allele-specific copy number analysis of whole-genome sequenced tumor tissue. Genome Biol. *14*, R24.

Miyahara, K., Kazama, H., Kokuba, H., Komatsu, S., Hirota, A., Takemura, J., Hirasawa, K., Moriya, S., Abe, A., Hiramoto, M., et al. (2016). Targeting bortezomib-induced aggresome formation using vinorelbine enhances the cytotoxic effect along with ER stress loading in breast cancer cell lines. Int. J. Oncol. *49*, 1848–1858.

Moolenaar, W.H., van Meeteren, L.A., and Giepmans, B.N. (2004). The ins and outs of lysophosphatidic acid signaling. BioEssays *26*, 870–881.

Moriya, S., Komatsu, S., Yamasaki, K., Kawai, Y., Kokuba, H., Hirota, A., Che, X.F., Inazu, M., Gotoh, A., Hiramoto, M., and Miyazawa, K. (2015). Targeting the integrated networks of aggresome formation, proteasome, and autophagy potentiates ER stress-mediated cell death in multiple myeloma cells. Int. J. Oncol. *46*, 474–486.

Nikolaev, S., Santoni, F., Garieri, M., Makrythanasis, P., Falconnet, E., Guipponi, M., Vannier, A., Radovanovic, I., Bena, F., Forestier, F., et al. (2014). Extrachromosomal driver mutations in glioblastoma and low-grade glioma. Nat. Commun. *5*, 5690.

Page, B., Page, M., and Noel, C. (1993). A new fluorometric assay for cytotoxicity measurements in-vitro. Int. J. Oncol. *3*, 473–476.

Pfaff, E., Remke, M., Sturm, D., Benner, A., Witt, H., Milde, T., von Bueren, A.O., Wittmann, A., Schöttler, A., Jorch, N., et al. (2010). TP53 mutation is frequently associated with CTNNB1 mutation or MYCN amplification and is compatible with long-term survival in medulloblastoma. J. Clin. Oncol. *28*, 5188–5196.

Pollard, S.M., Yoshikawa, K., Clarke, I.D., Danovi, D., Stricker, S., Russell, R., Bayani, J., Head, R., Lee, M., Bernstein, M., et al. (2009). Glioma stem cell lines expanded in adherent culture have tumor-specific phenotypes and are suitable for chemical and genetic screens. Cell Stem Cell *4*, 568–580.

Qiang, W., Sui, F., Ma, J., Li, X., Ren, X., Shao, Y., Liu, J., Guan, H., Shi, B., and Hou, P. (2017). Proteasome inhibitor MG132 induces thyroid cancer cell apoptosis by modulating the activity of transcription factor FOXO3a. Endocrine *56*, 98–108.

Reardon, D.A., Nabors, L.B., Mason, W.P., Perry, J.R., Shapiro, W., Kavan, P., Mathieu, D., Phuphanich, S., Cseh, A., Fu, Y., et al.; BI 1200 36 Trial Group and the Canadian Brain Tumour Consortium (2015). Phase I/randomized phase II study of afatinib, an irreversible ErbB family blocker, with or without protracted temozolomide in adults with recurrent glioblastoma. Neuro-oncol. *17*, 430–439.

Richardson, P.G., Sonneveld, P., Schuster, M.W., Irwin, D., Stadtmauer, E.A., Facon, T., Harousseau, J.L., Ben-Yehuda, D., Lonial, S., Goldschmidt, H., et al.; Assessment of Proteasome Inhibition for Extending Remissions (APEX) Investigators (2005). Bortezomib or high-dose dexamethasone for relapsed multiple myeloma. N. Engl. J. Med. *352*, 2487–2498.

Schindelin, J., Arganda-Carreras, I., Frise, E., et al. (2012). Fiji: an open-source platform for biological-image analysis. Nat Methods *9*, 676–682.

Schmidt, L., Baskaran, S., Johansson, P., Padhan, N., Matuszewski, D., Green, L.C., Elfineh, L., Wee, S., Häggblad, M., Martens, U., et al. (2016). Case-specific potentiation of glioblastoma drugs by pterostilbene. Oncotarget *7*, 73200–73215.

Seashore-Ludlow, B., Rees, M.G., Cheah, J.H., Cokol, M., Price, E.V., Coletti, M.E., Jones, V., Bodycombe, N.E., Soule, C.K., Gould, J., et al. (2015). Harnessing connectivity in a large-scale small-molecule sensitivity dataset. Cancer Discov. *5*, 1210–1223.

Seol, D.W. (2011). p53-Independent up-regulation of a TRAIL receptor DR5 by proteasome inhibitors: a mechanism for proteasome inhibitor-enhanced TRAIL-induced apoptosis. Biochem. Biophys. Res. Commun. *416*, 222–225.

Shannon, P., Markiel, A., Ozier, O., Baliga, N.S., Wang, J.T., Ramage, D., Amin, N., Schwikowski, B., and Ideker, T. (2003). Cytoscape: a software environment for integrated models of biomolecular interaction networks. Genome Res. *13*, 2498–2504.

Spiegelberg, D., Mortensen, A.C., Lundsten, S., Brown, C.J., Lane, D.P., and Nestor, M. (2018). The MDM2/MDMX-p53 antagonist PM2 radiosensitizes wild-type p53 tumors. Cancer Res. *78*, 5084–5093.

Strauss, S.J., Higginbottom, K., Jüliger, S., Maharaj, L., Allen, P., Schenkein, D., Lister, T.A., and Joel, S.P. (2007). The proteasome inhibitor bortezomib acts independently of p53 and induces cell death via apoptosis and mitotic catastrophe in B-cell lymphoma cell lines. Cancer Res. *67*, 2783–2790.

Stupp, R., Mason, W.P., van den Bent, M.J., Weller, M., Fisher, B., Taphoorn, M.J., Belanger, K., Brandes, A.A., Marosi, C., Bogdahn, U., et al.; European Organisation for Research and Treatment of Cancer Brain Tumor and Radiotherapy Groups; National Cancer Institute of Canada Clinical Trials Group (2005). Radiotherapy plus concomitant and adjuvant temozolomide for glioblastoma. N. Engl. J. Med. *352*, 987–996.

Subramanian, A., Tamayo, P., Mootha, V.K., Mukherjee, S., Ebert, B.L., Gillette, M.A., Paulovich, A., Pomeroy, S.L., Golub, T.R., Lander, E.S., and Mesirov, J.P. (2005). Gene set enrichment analysis: a knowledge-based approach for interpreting genome-wide expression profiles. Proc. Natl. Acad. Sci. USA *102*, 15545–15550.

Tao, W., and Levine, A.J. (1999). P19(ARF) stabilizes p53 by blocking nucleo-cytoplasmic shuttling of Mdm2. Proc. Natl. Acad. Sci. USA *96*, 6937–6941.

Taylor, O.G., Brzozowski, J.S., and Skelding, K.A. (2019). Glioblastoma multiforme: an overview of emerging therapeutic targets. Front. Oncol. *9*, 963.

Tujebajeva, R.M., Graifer, D.M., Karpova, G.G., and Ajtkhozhina, N.A. (1989). Alkaloid homoharringtonine inhibits polypeptide chain elongation on human ribosomes on the step of peptide bond formation. FEBS Lett. *257*, 254–256.

Verhaak, R.G., Hoadley, K.A., Purdom, E., Wang, V., Qi, Y., Wilkerson, M.D., Miller, C.R., Ding, L., Golub, T., Mesirov, J.P., et al.; Cancer Genome Atlas Research Network (2010). Integrated genomic analysis identifies clinically relevant subtypes of glioblastoma characterized by abnormalities in PDGFRA, IDH1, EGFR, and NF1. Cancer Cell *17*, 98–110.

Wang, K., Li, M., and Hakonarson, H. (2010). ANNOVAR: functional annotation of genetic variants from high-throughput sequencing data. Nucleic Acids Res. *38*, e164.

Wang, Q., Hu, B., Hu, X., Kim, H., Squatrito, M., Scarpace, L., deCarvalho, A.C., Lyu, S., Li, P., Li, Y., et al. (2017). Tumor evolution of glioma-intrinsic gene expression subtypes associates with immunological changes in the microenvironment. Cancer Cell *32*, 42–56.e6.

Wilkerson, M.D., and Hayes, D.N. (2010). ConsensusClusterPlus: a class discovery tool with confidence assessments and item tracking. Bioinformatics *26*, 1572–1573.

Wu, C., Su, J., Wang, X., Wang, J., Xiao, K., Li, Y., Xiao, Q., Ling, M., Xiao, Y., Qin, C., et al. (2019). Overexpression of the phospholipase A2 group V gene in glioma tumors is associated with poor patient prognosis. Cancer Manag. Res. *11*, 3139–3152.

Xie, Y., Bergström, T., Jiang, Y., Johansson, P., Marinescu, V.D., Lindberg, N., Segerman, A., Wicher, G., Niklasson, M., Baskaran, S., et al. (2015). The human glioblastoma cell culture resource: validated cell models representing all molecular subtypes. EBioMedicine *2*, 1351–1363.

Xue, Y., Barker, N., Hoon, S., He, P., Thakur, T., Abdeen, S.R., Maruthappan, P., Ghadessy, F.J., and Lane, D.P. (2019). Bortezomib stabilizes and activates p53 in proliferative compartments of both normal and tumor tissues *in vivo*. Cancer Res. *79*, 3595–3607.

Yang, L., and Zhang, H. (2018). Expression of cytosolic phospholipase A2 alpha in glioblastoma is associated with resistance to chemotherapy. Am. J. Med. Sci. *356*, 391–398.

Yang, W., Soares, J., Greninger, P., Edelman, E.J., Lightfoot, H., Forbes, S., Bindal, N., Beare, D., Smith, J.A., Thompson, I.R., et al. (2013). Genomics of drug sensitivity in cancer (GDSC): a resource for therapeutic biomarker discovery in cancer cells. Nucleic Acids Res. *41*, D955–D961.

Yang, W., Warrington, N.M., Taylor, S.J., Whitmire, P., Carrasco, E., Singleton, K.W., Wu, N., Lathia, J.D., Berens, M.E., Kim, A.H., et al. (2019). Sex differences in GBM revealed by analysis of patient imaging, transcriptome, and survival data. Sci. Transl. Med. *11*, eaao5253.

Yerlikaya, A., Okur, E., Baykal, A.T., Acilan, C., Boyaci, I., and Ulukaya, E. (2015). A proteomic analysis of p53-independent induction of apoptosis by bortezomib in 4T1 breast cancer cell line. J. Proteomics *113*, 315–325.

Yoo, Y.D., Lee, D.H., Cha-Molstad, H., Kim, H., Mun, S.R., Ji, C., Park, S.H., Sung, K.S., Choi, S.A., Hwang, J., et al. (2017). Glioma-derived cancer stem cells are hypersensitive to proteasomal inhibition. EMBO Rep. *18*, 150–168.

Zou, H., and Hastie, T. (2005). Regularization and variable selection via the elastic net. J. R. Stat. Soc. Series B Stat. Methodol. *67*, 301–320.

STAR★METHODS

KEY RESOURCES TABLE

REAGENT or RESOURCE	SOURCE	IDENTIFIER
Antibodies		
Ubiquitin (P4D1) Mouse monoclonal antibody	Cell Signaling Technology	Cat#3936s; RRID:AB_2315523
Beta-Actin (C4) mouse monoclonal antibody	Santa Cruz	Cat#sc-47778, RRID:AB_626632
53BP1 Polyclonal Antibody	Invitrogen	Cat#PA554565; RRID:AB_2637496
P21-antibody rabbit antibody (12D1)	Cell signaling Technology	Cat#2947; RRID:AB_823586
Cyclophilin rabbit polyclonal antibody	Abcam	Cat# Ab16045; RRID:AB_443295
Anti-NuMA antibody	Abcam	Cat#97585; RRID:AB_10680001
Alexa Flour 488 Phalloidin	Thermofisher Scientific	Cat#A12379; RRID:AB_2315147
Alexa Flour 555 Goat anti mouse IgG	Invitrogen	Cat#A21422; RRID:AB_2535844
Alexa Flour 488 Goat anti rabbit IgG	Invitrogen	Cat#A11008; RRID:AB_143165
Alexa Flour 555 Donkey anti rabbit IgG	Invitrogen	Cat#31572-A; RRID: AB_162543
FITC Goat anti rabbit IgG	Jackson Immunoresearch	Cat#111-095-144; RRID:AB_2337978
Goat anti rabbit IgG antibody, HRP conjugate	Millipore	Cat#AP307P; RRID:AB_92641
Goat anti mouse IgG antibody, HRP conjugate	Millipore	Cat#AP308P; RRID: AB_11215796
Chemicals, Peptides, and Recombinant Proteins		
Screen-Well® kinase inhibitor library (80 compounds)	BIOMOL International/Enzo Life Sciences	Cat#BML-2832-0100
NCI DTP repository (101 compounds)	National Cancer Institute (NCI)/ Division of Cancer Treatment and Diagnosis (DCTD)/Developmental Therapeutics Program (DTP)	https://dtp.cancer.gov; RRID:SCR_003057
NIH clinical collection (727 compounds)	NIH Molecular Libraries and Imaging program	https://www.nihclinicalcollection.com/
Prestwick Chemical Library® (1200 compounds)	Prestwick Library	https://www.prestwickchemical.com/prestwick-chemical-library.html
Bortezomib	Selleck Chemicals	Cat#S1013; CAS:179324-69-7
Marizomib	Sigma Aldrich	Cat#SML1916; CAS:4337742-34-2
Navitoclax	Selleck Chemicals	Cat#S1001; CAS: 923564-51-6
Milciclib (PHA-848125)	Selleck Chemicals	Cat#S2751 CAS:802539-81-7
Costunolide	Selleck Chemicals	Cat#S1319; CAS: 553-21-9
PM2	David P. Lane Lab (A*Star, Singapore)	N/A
VIP-116	David P. Lane Lab (A*Star, Singapore)	N/A
Carfilzomib	Selleck Chemicals	Cat#S2853; CAS:868540-17-4
Oprozomib	Selleck Chemicals	Cat#S704901; CAS:935888-69-0
Ixazomib	Selleck Chemicals	Cat#S2181; CAS:1201902-80-8
Delanzomib	Selleck Chemicals	Cat#S1157; CAS:847499-27-8
MG-132	Selleck Chemicals	Cat#2619; CAS:133407-82-6
Torin 2	Selleck Chemicals	Cat#S2817; CAS:1223001-51-1
Myricetin	Selleck Chemicals	Cat#S2326; CAS:529-44-2
Spectinomycin 2HCl	Selleck Chemicals	Cat#S2510; CAS:21736-83-4
Cilnidipine	Selleck Chemicals	Cat#S1293; CAS:132203-70-4
Etoposide	Selleck Chemicals	Cat#S1225; CAS: 33419-42-0
N-acetyl-L-cysteine	Sigma Aldrich	Cat#A9165; CAS:616-91-1
7-AAD	BD Biosciences	Cat#559925
BD Perm/Wash™ buffer	BD Biosciences	Cat#554723

(*Continued on next page*)

Continued

REAGENT or RESOURCE	SOURCE	IDENTIFIER
Neurobasal Medium	GIBCO	Cat#21103049
Neurobasal medium (without phenol red)	GIBCO	Cat#12348017
DMEM/F-12 GlutaMAX Supplement	GIBCO	Cat#31331028
DMEM/F-12 GlutMAX Supplement without phenol red	GIBCO	Cat#21041025
B-27 Supplement (50X), minus vitamin A	GIBCO	Cat#12587010
B-27 Supplement (50X), minus antioxidants	GIBCO	Cat#10889038
HBSS calcium, magnesium no phenol red	GIBCO	Cat#14025050
N-2 Supplement (100X)	GIBCO	Cat#17502001
StemPro Accutase Cell Dissociation Reagent	GIBCO	Cat#A1110501
Laminin from Engelbreth-Holm-Swarm murine sarcoma basement membrane	Sigma-Aldrich	Cat#L2020-1MG; CAS: 114956-81-9
Animal-Free Recombinant Human EGF	PeproTech	Cat#AF-10015
Animal-Free Recombinant Human FGF-basic (154 a.a)	PeproTech	Cat#AF-10018-B
Penicillin-Streptomycin	Sigma-Aldrich	Cat#P0781
DMEM, without methionine	Thermo Fisher Scientific	Cat#21013-024
Poly-L-ornithine (0.01% sterile filtered) solution	Sigma-Aldrich	Cat#P4957
RIPA Lysis and Extraction Buffer	Thermo Fisher Scientific	Cat#89900
Triton X-100	Sigma-Aldrich	Cat#X100
Tween 20	Sigma-Aldrich	Cat# P1379
Bovine serum albumin fraction V	Sigma-Aldrich	Cat#10735099001
Paraformaldehyde 16% (w/v), in aqueous solution methanol free	Alfa Aesar	Cat#AA43368
Phosphate Buffered Saline (PBS) Ultra pure grade	Amresco	Cat# 0780
TBS, 20X ready -pack Ultra pure	Amresco	Cat# 0788-2K
HOECHST 33342	Invitrogen	Cat# 62249
NuPAGE 4-12% Bis-Tris Gel	Invitrogen	Cat# NP0321
NuPAGE MES Running buffer (20X)	Invitrogen	Cat#NP0002
NuPAGE MOPS Running buffer (20X)	Invitrogen	Cat#NP0001
Restore western blot stripping buffer	Thermo Fisher Scientific	Cat#21059
iBLOT Gel transfer stacks Nitrocellulose, Mini	Invitrogen	Cat#IB301002
Viraductin Lentivirus Transduction Kit	Cell Biolabs	Cat#LTV-201
Isoba® vet (isoflurane)	Baxter	Cat#014083
Carprofen	Orion Pharma Animal Health	N/A
Luciferin	Promega	Cat#E1605
D-Luciferin, sodium salt (Proven and Published)	Zellbio	Cat# LUCNA-250
4% phosphate buffered formaldehyde	Histolab	Cat#02176; CAS:50-00-0
Antigen unmasking solution	Vector Laboratories	Cat#H-3300
DAB Quanto	Thermo Fisher Scientific	Cat#TA-060-QHDX
Mounting medium for light microscopy Pertex®	Histolab	Cat#00811
Corning® growth factor reduced Matrigel® matrix	VWR	Cat#734-0269
Corning Matrigel Membrane Matrix	Fisher Scientific	Cat#11543550
Dimethyl Sulfoxide	Millipore	Cat#317275
Critical Commercial Assays		
Cytoscan™ HD Arrays	Thermo Fisher Scientific	Cat#901833
Cytoscan Reagent kit	Thermo Fisher Scientific	Cat#901808
Titanium® DNA Amplification Kit	Clontech	Cat#639240
GeneChip™ HTA 2.0 Arrays	Thermo Fisher Scientific	Cat#902162
Infinium® MethylationEPIC BeadChip Kit	Illumina	Cat#WG-317-1002

(*Continued on next page*)

Continued

REAGENT or RESOURCE	SOURCE	IDENTIFIER
EZ-96 DNA Methylation Kit	Zymo Research	Cat#D5003
Qubit dsDNA HS Assay Kit	Thermo Fisher Scientific	Cat#Q32851
Genomic DNA ScreenTape	Agilent	Cat#5067-5365
Genomic DNA Reagents	Agilent	Cat#5067-5366
miRNeasy Mini Kit	QIAGEN	Cat#217004
DNeasy Blood and Tissue Kit	QIAGEN	Cat#69506
Alamar blue cell viability reagent	Invitrogen	Cat#DAL1100
Pierce™ BCA Protein Assay Kit	Thermo Fisher Scientific	Cat#23225
ECL Select western blotting detection reagent	GE healthcare	Cat#RPN2235
SuperSignal West Femto maximum sensitivity substrate	Thermo Fisher Scientific	Cat#34094
Caspase - Glo 3/7 Assay Systems	Promega	Cat#G8091
GSH/GSSG - Glo Assay	Promega	Cat#V6611
Click-iT® HPG Alexa Fluor® 488 Protein Synthesis Assay Kit	Thermo Fisher Scientific	Cat#C10428
iScript gDNA Clear cDNA synthesis kit	Bio-Rad	Cat#1725034
Protease Inhibitor Cocktail cOmplete mini	Sigma-Aldrich	Cat#000000011836153001
Olink Incubation Stabilizer	Olink Proteomics	Cat#84008
Olink Incubation Solution	Olink Proteomics	Cat#84009
Olink PEA Solution	Olink Proteomics	Cat#84002
Olink PEA Enzyme	Olink Proteomics	Cat#84003
Olink Detection Solution	Olink Proteomics	Cat#84015
Olink Detection Enzyme	Olink Proteomics	Cat#84005
Olink PCR Polymerase	Olink Proteomics	Cat#84004
96.96 Dynamic Array Integrated Fluidic Circuit	Fluidigm	Cat#BMK-M-96.96
Proteasome 20S activity kit	Promega	Cat#G8621
GIBCO human neural stem cell (H9) kit	Invitrogen	Cat#N7800200
CM-H2DCFDA (general oxidative stress indicator)	Invitrogen	Cat#C6827
FITC-BrdU Flow kit	BD PharMingen	Cat#559619
SsoAdvanced Universal SYBR	Bio-Rad	Cat#1725275
ProLong Diamond antifade mountant	Invitrogen	Cat#P36961
Deposited Data		
Gene Expression Omnibus repository	This paper	https://www.ncbi.nlm.nih.gov/geo/query/acc.cgi?acc=GSE152160
Experimental Models: Cell Lines		
Patient-derived glioblastoma cell cultures; see Table S1	HGCC biobank	Authenticated by STR analysis by HGCC
Human: Immortalized astrocytes	From Arne Östman Lab (Karolinska Institutet, Sweden)	N/A
Human: Foreskin fibroblasts AG 1523	From Karin Forsberg-Nilsson Lab (Uppsala University, Sweden)	N/A
Human: HepG2	From Bo Lundgren Lab (Stockholm University, Sweden)	N/A
Human: H9-derived neural stem cells	Life Technologies	Cat#510088, Lot#1206001
Experimental Models: Organisms/Strains		
Balb/cAnNRj-Foxn1nu/Foxn1nu mice, female mice aged 7-9 weeks	Janvier Labs	N/A
White Leghorn chicken eggs	LSK Poultry Oy, Laitila, FL	N/A

(*Continued on next page*)

Continued

REAGENT or RESOURCE	SOURCE	IDENTIFIER
Oligonucleotides		
qPCR primers; see Table S5	This study	N/A
Recombinant DNA		
pBMN(CMV-copGFP-Luc2-Puro)	Jin et al., 2016	Cat#80389; RRID:Addgene_80389
Software and Algorithms		
ImageJ (FIJI version 1.0) https://imagej.nih.gov/ij/	Schindelin et al., 2012	https://imagej.nih.gov/ij/
IndiGo version 2.0.5.0	Berthold Technologies	https://indigo.onki.de/indigo.html
IncuCyte Zoom 2016A Live image analysis software	Essen Biosciences Inc.	N/A
IncuCyte ® S3 Spheroid Analysis software	Essen Biosciences Inc.	N/A
IncuCyte ®Basic Analysis Software (v2019B)	Essen Biosciences Inc.	N/A
Living Image 3.2.0 software	PerkinElmer	N/A
qBase MS Excel VBA applet	Hellemans et. al., 2007	N/A
GraphPad Prism 6 or Prism 8	GraphPad software	https://www.graphpad.com/scientific-software/prism/; RRID: SCR_002798
Bio-Rad CFX Manager Software	Bio-Rad	N/A
CytExpert software version 2.4	Beckman Coulter	N/A
SnapGene Viewer 4.1.9 software	GSL Biotech LLC	N/A

RESOURCE AVAILABILITY

Lead Contact

Further information and requests for resources and reagents should be directed to and will be fulfilled by the Lead Contact, Sven Nelander (sven.nelander@igp.uu.se).

Materials Availability

Individual cell cultures can be obtained following establishment of a Material Transfer Agreement. Contact the Human Glioma Cell Culture biobank administrator at mail@hgcc.se, or the Lead Contact. GFP-tagged versions of the cell cultures used in the CAM experiments are obtained using the same procedure.

Data and Code Availability

Individual genomic data types are made available at portal.hgcc.se. The accession number for the gene expression data reported in this paper is Gene Expression Omnibus: GSE152160. Code for computational analyses are available from the Lead Contact.

EXPERIMENTAL MODEL AND SUBJECT DETAILS

Tumor sample collection was approved by the Uppsala regional ethical review board, number 2007/353; informed consent was obtained from all subjects included. The cell culture designations and key data (sex, age, survival) of each subject are listed in Table S1. All mouse experiments were performed in compliance with an ethical permit granted by the Uppsala Animal Research Ethical Board, number C41/14. Mice used were Balb/cAnNRj-Foxn1nu/Foxn1nu female mice from Janvier Labs, 7 weeks old at the start of the experiment. Mice were housed in individually ventilated cages (5 mice per cage) with appropriate paper housing enrichments, bedding material and provided with food and drinking water *ad libitum* with a 12/12-hour light/dark cycle.

Cell culture collection methods

Primary cultures were derived from tumor samples in defined serum-free neural stem cell (NSC) medium, supplemented with B-27, N2, EGF, FGF, on laminin-coated Corning Primaria Cell Culture plates (Thermo Fisher Scientific, Waltham, MA) as described (Xie et al., 2015), and GBM cells (Table S1) were subsequently grown in this medium. The cell cultures for the drug screening assay were between passage 8 and 24 (average 16). As reference cell lines, we used human immortalized astrocytes (Arne Östman, Karolinska Institutet), HepG2 (Bo Lundgren, Stockholm University) and human foreskin fibroblasts 1523 (Karin Forsberg Nilsson, Uppsala University). References cells were grown as adherent cultures in DMEM culture medium (Invitrogen, Carlsbad, CA) supplemented with 1% L-Glutamine (Sigma-Aldrich, St. Louis, MO), 1% Penicillin/Streptomycin (Sigma-Aldrich), 1% GIBCO MEM Non-Essential Amino Acids (Thermo Fisher Scientific) and GIBCO 10% fetal bovine serum (Thermo Fisher Scientific). H9-derived human

neural stem cells, propagated as adherent culture in complete StemPro® NSC SFM (A1050901, Thermo Fisher Scientific) according to manufacturer instructions were also included as a reference.

METHOD DETAILS

Genomic profiling of patient-derived GBM cultures

Genomic profiling of the GBM cell cultures (Figure 1C; Figure S1) was conducted at Science for Life Laboratory core facilities (scilifelab.se) and the Uppsala Academic Hospital Array and Analysis facility. DNA was amplified from cell cultures using the DNeasy Blood and tissue kit (QIAGEN). DNA copy number aberrations were measured using Affymetrix Cytoscan HD arrays (Thermo Fisher Scientific) in accordance with the manufacturer's instructions (Affymetrix® Cytoscan User Guide (P/N 703038 Rev4.). Chromosomal segments carrying altered numbers of copies was estimated using the Patchwork R package (Mayrhofer et al., 2013), which quantifies the log-relative change in DNA content for each chromosomal region. DNA whole exome sequencing of cell cultures was performed using Ion Torrent sequencing as follows. 100 ng of genomic DNA was amplified according to the Ion AmpliSeqExome Library Preparation protocol (Thermo Fisher Scientific). Adaptors (Ion P1 Adaptor and Ion XpressBarcode Adaptor, Thermo Fisher Scientific) were then ligated to generate sequencing libraries, which were purified using Agencourt® AMPure® XP reagent (Beckman Coulter), eluted in amplification mix (Platinum® PCR SuperMix High Fidelity and Library Amplification Primer Mix, Thermo Fisher Scientific) and then amplified. Size-selection and purification was conducted using Agencourt® AMPure® XP reagent (Beckman Coulter). Emulsion PCR was performed on the Ion OneTouch2 system using the Ion PITemplate OT2 200 Kit v3 (Thermo Fisher Scientific). Samples were loaded on Ion PIchips v2 and sequenced on the Ion ProtonSystem using Ion PISequencing 200 Kit v3 chemistry (Thermo Fisher Scientific). Data were analyzed with the Torrent Suite Software (Thermo Fisher Scientific). Following alignment to the hg19 reference genome using BowTie, we computed somatic variants using Torrent Suite, SomaticSniper (Larson et al., 2012), VarScan2 (Koboldt et al., 2012) and MuTect 2 (Cibulskis et al., 2013) using default settings. We annotated the variants using ANNOVAR (Wang et al., 2010) and dbsnp138 (https://www.ncbi.nlm.nih.gov/projects/SNP/). The calls were aggregated across the four callers and a gene was considered mutated (1) if it met the criteria of (i) being found by at least 2 callers, (ii) was annotated as nonsynonymous, and (iii) not present as a germline variant in the 1000 genomes project (1000 Genomes Project Consortium et al., 2015) above 2 percent prevalence according to ANNOVAR. DNA methylomes were measured on Infinium® MethylationEPIC BeadChip Infinium arrays (Illumina), in accordance with the Infinium® HD Assay Methylation protocol (Illumina). Quality control of the generated data was performed using the methylation module of the GenomeStudio® v2011.1 data analysis software (Illumina) and by use of the BeadArray Controls Reporter software (Illumina) to analyze the sample controls. From the primary data, probe specific β values, for 850,000 probes were computed as the probe-specific methylation fraction. RNA profiling was performed using Affymetrix HTA 2.0 arrays according to manufacturer recommendations, and normalized to gene level using the Affymetrix Power Tools version 1.19.0 (https://www.affymetrix.com). The resulting gene expression data were normalized using the naiveReplicateRUV method (Gagnon-Bartsch and Speed, 2012) with negative control genes defined as in Eisenberg and Levanon (2003).

Pharmacological profiling of patient-derived GBM cultures

Large-scale measurements of drug responses (Figure 2) were carried out at the Science for Life Laboratory Drug Discovery and Development platform. Cells were seeded one day prior to treatment using a Multidrop 384 liquid dispenser (Thermo Fisher Scientific) in laminin-coated 384-well microplates (BD Falcon Optilux #353962), at a density ranging from 2000-4000 cells per well to ensure subconfluent growth phase (approximately 70%) at the end of the assay. For the initial screen in 9 glioblastoma cell cultures (Figure 2A) we tested 1544 unique compounds from the Screen-Well® kinase inhibitor library (BIOMOL International/Enzo Life Sciences, 80 compounds), the NCI DTP Repository (National Institute of Health, 101 compounds), the NIH clinical collection (https://commonfund.nih.gov/molecularlibraries/tools, 727 compounds), and the Prestwick Chemical Library® (Prestwick Chemical, 1200 compounds). Redundant compounds were removed to a total of 1544 compounds. In the subsequent screen (c.f. Figure 2A) 262 compounds were tested in 11-point dose dilution series (starting at 100M in Phase 2 and 50M in Phase 3) and assayed for viability after 3 days of treatment using a Resazurin assay diluted 1:10 in medium as previously described (Page et al., 1993), and detected by a fluorescent plate reader (EnVision multilabel reader, PerkinElmer). Each plate was subject to quality control comparing fluorescence values of doxorubicin treated (11 doses, 0-100 M) cells as positive control and DMSO vehicle (0.1%) as negative control. All data was normalized against plate DMSO vehicle wells. We scored the sensitivity of each cell culture to each compound by an Area Under the Curve (AUC) score for the dose-response values. This metric was used since it gives an interpretable value for all drugs and cell cultures, not only for those with well-defined IC_{50}. For 183/262 compounds, the IC_{50} was within the 11 dose range and for an additional 16 drugs, the IC75 was within the dose range used (Table S2).

Gene signature of p53 activity in GBM, and analysis of p53 status in 10 GBM cultures

For all GBM cultures with available whole-exome sequencing and RNA profiling data (n = 62) we computed the differential expression between p53 mutant and p53 wild-type cell cultures, detecting p53 as the main differentially expressed pathway. The 36 transcripts in the p53 Hallmark pathway that were differentially expressed (BH adjusted $p<0.05$) were arranged as a matrix, which was analyzed by

PCA, whereby the first principal component was used as the p53 signature score of each cell culture (Figure 4A). We selected 10 representative GBM cultures based on variation in this p53 signature and proteasome inhibitor response (Figure 5A). To confirm p53 status, we used targeted Sanger sequencing (c.f. . For each of the 10 selected cultures, we amplified DNA sequences for p53 coding exons as described by Pfaff et al. (2010). The sequencing was performed as Light run in forward direction by GATC Biotech using 5 l of PCR products and sequence alignment was carried out using the SnapGene Viewer 4.1.9 software (GSL Biotech LLC) against the NC_000017.11 TP53 reference sequence. The International Agency for Research on Cancer TP53 database (https://p53.iarc.fr/) was used to determine the significance of identified sequence variants. As a complement to Sanger sequencing, p53 functional status was assessed using an etoposide treatment assay (Figure S4B), as follows. The selected 10 GBM cell cultures were treated with 10 M etoposide for 2, 6, 16 and 24 hr, following lysis in RIPA buffer (Thermo Fisher Scientific) supplemented with cOmpleteULTRA protease inhibitor cocktail (Roche) and phosphatase inhibitors PhosSTOP (Roche). 25 μg of lysate was resolved by 4%–12% Bis-Tris gradient gel (Invitrogen) in MOPS buffer, transferred onto nitrocellulose membranes (Invitrogen) and blocked in buffer (5% (wt/vol) BSA or 5% (wt/vol) nonfat milk (Bio-Rad), TBST (TBS, pH 7.4, 0.1% Tween-20) for 1 hr at room temperature. Primary antibodies used were p21 rabbit antibody (12D1, Cell Signaling Technology) (1:1000 in 5% BSA, TBST), beta-actin mouse monoclonal antibody (C4, Santa Cruz) (1:1000 in 5% milk, TBST) and cyclophilin rabbit polyclonal antibody (ab16045, Abcam) (1:2000 in 5% milk/TBST). Following overnight incubation of membranes with primary antibody at 4C; HRP-linked secondary antibodies were diluted in blocking buffer; donkey anti-rabbit (GE Healthcare, Chicago, IL) (1:5000 in 5% BSA), goat anti-mouse (GE Healthcare) (1:5000 in 5% milk), and incubated for 1 hour at room temperature. Blots were developed by Amersham™ECL Select™ western blotting detection reagent (GE Healthcare), and visualized using ImageQuant LAS 4000 (GE Healthcare) biomolecular imager.

RNA profiling and GSEA

For Figure 5B, we used RNA sequencing using the method in Almstedt et al. (2020) to profile U3013MG and U3180MG cells after 6 hr treatment by bortezomib, marizomib and delanzomib at 10nM (n = 3 technical replicates for each treatment). Vehicle treated cells were used as replicates (n = 3 technical replicates). We used Fisher's test with FDR p value correction to test for overlap between Hallmark pathways and genes that were either upregulated in both cell cultures (average fold change in both) or selectively up in U3180MG versus U3013MG (fold change in U3180MG cells minus the fold change in U3013MG cells).

Responses to proteasome inhibition in 10 GBM cultures with different p53 status

To measure the effects of proteasome inhibition, we used qPCR, western blot and proximity extension assays as follows. For Figure S4A, we selected a panel of genes for qPCR validation. Selection was based on whether (i) they were a marker in our network analysis, (ii) they were a known p53 target or (iii) involved in other key pathways. A panel of 10 GBM cultures with different proteasome inhibitor sensitivity were treated with 10nM bortezomib (PS-341, #S1013, Selleck Chemicals) or vehicle (0.1% DMSO) for 6 hr and 24 hr in triplicates. Total RNA was isolated using the phenol/chloroform method with TRIzol LS Reagent (#10296010, Thermo Fisher Scientific) and 500 ng of total RNA was then transcribed using iScript™ gDNA Clear cDNA Synthesis Kit (Bio-Rad). Quantitative PCR was carried out on a CFX384 Touch™ Real Time PCR Detection System (Bio-Rad), using SsoAdvanced™ Universal SYBRGreen Supermix (#1725275, Bio-Rad) in duplicates in a total reaction volume of 10 l, using primers in Table S5. Gene expression was normalized using 3 reference genes (RPS18, GAPDH, RLP13A) and calculated with qBase MSExcel VBA applet (Hellemans et al., 2007). To analyze protein turnover in treated versus untreated resistant and non-resistant cells (Figure S4C), we analyzed detergent soluble and insoluble fractions, for enrichment of aggregated protein (Miyahara et al., 2016; Moriya et al., 2015) after 24 hours of bortezomib treatment, by western blot detection of ubiquitin (P4D1, Cell Signaling Technology, Inc. 1:1000 in blocking buffer) with b-actin (C4, Santa Cruz, 1:10000 in blocking buffer) as a loading control. Blots were developed and visualized as described above.

Details of proximity extension assay analysis

Proteome alterations (Figure 4C; Figure S4E) were measured on proximity extension assay (PEA) arrays (Olink Proteomics), as follows. Cell cultures U3013MG, U3054MG, U3008MG, and U3213MG were seeded at 15,000 cells per well in two replicate 96-well plates [Greiner Bio One cat#655986]. Twenty-four hr later, bortezomib was added at a final concentration of 1 nM, 6 nM, 10 nM or 0.2% DMSO as vehicle control. At 24 hr post-drug exposure, the replicate plates were gently washed 1X with PBS (37°C). Subsequently, the cells in one 96-well plate were fixed at room temperature for 10 min with a mixture of 2% PFA, 0.1% Triton X-100 and 10 g/ml Hoechst stain. The fixed cells were to enumerate the number of cells per well per corresponding treatment regimen. The cells in the second plate were lysed with 25l ice-cold lysis buffer/well (1% NP-40, 0.1% Triton X-100, 0.1% sulfobetaine, 150 mM NaCl, Protease Inhibitor Cocktail cOmpletemini (Roche), TE pH 8). Following the addition of the lysis buffer, the plate was briefly vortexed, centrifuged for 1 min, 4°C at 1000 rpm, and then stored at −80°C until use. The cell lysates were analyzed for relative protein expression using two non-commercial, exploratory multiplex proximity extension assay (PEA) panels (Olink Proteomics). The two panels target proteins involved in cancer-related pathways and cellular processes (e.g., cell cycle) respectively. Each PEA panel includes 92 assays targeting proteins and four spike-in controls consisting of two recombinant non-human proteins as incubation controls, an extension control (ExtCtl) and a PCR/detection control. Briefly, 2l cell lysate was mixed with 3l multiplex PEA probe mix. The

mix contained 0.3l of each the PEA A- and B-oligonucleotide conjugated antibody probes (final antibody-conjugate concentration of 100 pM), 0.2l Incubation Stabilizer (Olink Proteomics), and 2.1l Incubation Solution (Olink Proteomics). Each analysis plate included 8 replicate lysis buffer-only negative controls. The plates were briefly centrifuged, sealed, and incubated overnight at 4°C. Following overnight incubation, plates were briefly spun down, and 96 mL of a PEA probe extension mix was added to each well. The mix contained 0.2l PCR Polymerase, 0.5l PEA Enzyme, and 10l PEA Solution (all Olink Proteomics) and 85.3l molecular grade water. Plates were sealed, gently vortexed, spun down, and then placed in a thermal cycler for the extension reaction (50°C, 20 min) and pre-amplification of extended PEA probes via universal primers (95°C, 5 min; 95°C, 30 s; 54°C, 1 min; and 60°C, 1 min) for 17 cycles. The pre-amplified DNA molecules from the multiplex detection reaction were decoded and quantified using a Fluidigm 96.96 Dynamic Array Integrated Fluidic Circuit on a Biomark HD system. 2.8l of each sample was mixed with 5l Detection Solution, 0.071l Detection Enzyme, and 0.028l PCR Polymerase (all Olink Proteomics) and 2.1l molecular grade water. 5l of each sample plus detection mix was loaded into a primed 96.96 Dynamic Array IFC (right inlets). 5l of each of the 96 primer pairs (Olink Proteomics), designed to amplify individual target-specific DNA reporter sequences generated in the PEA reactions, was also loaded in the Dynamic Array (left inlets). The chip was placed in Fluidigm's IFC HX according to the manufacturer's instructions and then run in Fluidigm's Biomark with the following settings (Gene Expression application, ROX passive reference, single-probe assay with FAM-MGB probe) and protocol: thermal mix (50°C, 120 s; 70°C, 1,800 s; 25°C, 600 s), hot start (95°C, 300 s), and PCR cycling for 40 cycles (95°C, 15 s; 60°C, 60 s). BioMark generated PEA output files were processed to flag data points where the ExtCtl was smaller or greater than two standard deviations from the ExtCtl sample mean. The remaining Ct values were normalized as follows: for each sample, the Ct value of the ExtCtl was subtracted from the Ct value of the protein analyte yielding dCt values. Then, for each assay, the dCt values were subtracted from a negative control background value computed as the mean - 3*SD of the lysis buffer only negative control values. This ensures that observed signals for each assay in the presence of a cell are at least 3 standard deviations away from any signals observed in the absence of any antigen. All resulting values below zero were set to zero, and the signal was deemed undetected. We analyzed the data using a linear model for each protein (MATLAB fitlme) to estimate effects corresponding to the (log2) differential protein expression between resistant and sensitive cells (shown in Figure 4C) and the effect of bortezomib (shown in Figure S4E).

p53 targets and ROS levels in proteasome inhibitor-treated GBM cultures

To measure the level of reactive oxygen species before and after treatment (Figure 5C), we seeded GBM cells to Corning 96-well black wall plates at the concentration of 10.000 cells per well in NSC medium where B27 supplement was replaced with B27 Supplement, minus antioxidants (10889-038, Thermo Fisher Scientific). After overnight incubation, cells were treated with etoposide (10, 30 and 50 M) and bortezomib (10 nM) for 30 hr. For assessment of general reactive oxygen species, cell-permeant fluorescent probe CM-H2DCFDA (#C6827, Thermo Fisher Scientific) was used at 2.5 M final concentration, and cells were imaged by an IncuCyte® S3 live-cell imaging system (Sartorius). Acquired images were analyzed with the IncuCyte® inbuilt software to determine average green mean object intensity (GCU). The experiment was performed in three biological replicates with four technical replicates each, for a panel of ten GBM cell cultures.

Glutathione ratio and caspase 3/7 assays

We measured bortezomib-induced cellular stress (Figure 5D) using the luminescence-based GSH/GSSG-Glo assay (Promega). Both oxidized and total glutathione levels were obtained and used to calculate the ratio of reduced to oxidized glutathione. Cells were seeded at 5,000 cells/well. After 24 hours, cells were treated with either the drug bortezomib at 10 nM or the vehicle for 72 hours. Triplicate wells were used per condition. Luminescence was measured following the manufacturer's instructions, and background values were subtracted from all measurements. The ratios of GSH/GSSH were calculated for vehicle and control-treated cells. To measure Caspase 3/7 activity (Figure 5E), cells were seeded overnight at 5,000 cells/well in laminin-coated 96-well Primaria plates in standard NSC medium. Cells were then incubated for 48 hours with bortezomib (10 nM), the corresponding DMSO concentration, or left untreated. Triplicate wells were used per condition. Viability assay was performed using the alamarBlue® cell viability reagent. Measurement of caspase 3 and 7 levels was performed using the Caspase-Glo® 3/7 Assay detection assay kit (Promega) following manufacturer recommendations. As above, cells were seeded overnight in a white-walled 96-well plate at 5.000 cells/well following incubation for 48 hr in triplicate with bortezomib (10 nM), vehicle or left untreated. An equal volume of reconstituted Caspase-Glo Reagent was added to each well and luminescence was measured after 30 min incubation. Background luminescence was subtracted. The amount of Caspase 3/7 was then calculated relative to cell viability for each cell culture.

Chicken chorioallantoic membrane assay

For Figures 6A–6C, fertilized White Leghorn chicken eggs were obtained within a week after laying (LSK Poultry Oy). The highest non-toxic dose of bortezomib was established to be approximately 10 g/kg. On EDD 7, $1x10^6$ glioblastoma cells were transplanted onto the CAM in 20 l of 50% Matrigel™ (#11543550, Fisher Scientific) and PBS suspension. On EDD 10, we recorded bioluminescent (BLI) signal using an IVIS Spectrum camera (PerkinElmer) and applied vehicle (0.01% DMSO) or bortezomib (5 or 10 g/kg) topically on the CAM. On EDD 12, IVIS imaging was repeated and embryos were euthanized. BLI signal was analyzed using Living Image 3.2.0 (PerkinElmer) software and we used linear regression to estimate the log fold IVIS signal per g/kg unit of treatment, with data from n = 322 eggs in total.

Mouse xenotransplantation and bortezomib treatment

All mouse experiments were performed in compliance with an ethical permit granted by the Uppsala Animal Research Ethical Board, number C41/14. All animals were housed in individually ventilated cages (5 mice per cage) with appropriate paper housing enrichments, bedding material and provided with food and drinking water *ad libitum* with 12/12-hour light/dark cycle. 7 week-old Balb/cAnNRj-Foxn1nu/Foxn1nu female mice (Janvier Labs) were injected with U3013MG cells cultured adherently, U3013MG cultured as spheres and U3008MG cultured as spheres. When tumor volume exceeded 0.1 cm^3, mice were randomized into groups treated with bortezomib (0.5 mg/kg) or vehicle (DMSO). We used 7 mice per treatment and cell line. After tumor induction with PI-sensitive and PI-resistant glioblastoma cell cultures, mice were monitored at least twice per week. Weights were taken once per week initially and three times weekly once tumors developed. Tumors were measured three times weekly by caliper and tumor volume was calculated according to (length x $width^2$)/2. Treatments were administered twice a week by intraperitoneal injection. All animals were euthanized once the tumor volume reached 1000 mm^3 or after a maximum of 4 weeks of treatment. In the analysis, mice injected with adherently and sphere grown U3013MG were pooled and data was analyzed using a linear model implemented using MATLAB fitlme (Wilkinson notation volume ~+ time + time:bortezomib, reported p value in Figure 6D corresponding to the time:bortezomib interaction term).

Modulation of proteasome inhibitor responses by heat, antioxidants and potentiating drugs

To measure whether antioxidants or heat-induced accumulation of ROS could have a protecting or potentiating effect in bortezomib treated GBM cells, we analyzed their viability in drug pair combination assays. Primary GBM cultures were treated by vehicle, bortezomib (10nM), or combination of bortezomib (10 nM) with N-acetylcysteine (1 mM, Sigma-Aldrich) or myricetin (200 M, Selleck Chemicals). The effect of heat on bortezomib treated GBM cells was assessed by inducing 42C heat shock during 4 hours concomitantly with bortezomib (10 nM) addition (Figure S4D). For each cell culture, cells were seeded in separate plates for control (37°C) and heat treatment (42°C). Primaria 96-well plates (VWR) were coated with laminin and incubated for 30 min at 37°C, before 5000 cells per well were seeded and incubated overnight at 37°C before treatment. For each cell culture, bortezomib (22 nM) and corresponding control DMSO were added to all plates, and the heating plates were incubated at 42°C for 4-, 24- and 48 hours, while their individual control plates were incubated at 37°C. Viability read was performed using the Wallac Victor 1420 multilabel counter (Perkin Elmer). To assess potential synergism between bortezomib and other compounds (Figures 7A–7E), 10 GBM cultures were seeded in 96 well plates 5.000 cells/well and allowed to attach overnight. The next day, two proteasome inhibitors, bortezomib were added in 6x6 pairwise combinations with 25 drugs identified in our integrative data analysis (drugs and dose ranges in Table S6). The highest concentration of each drug was set to around twofold the IC_{50} value identified in the literature. Cells in the control wells were treated with DMSO (0.1 %, corresponding to 10 M drug; or highest concentration of the drug dilutions, but not exceeding 0.3 %). After 72h incubation alamarBlue® cell viability reagent (Thermo Fisher Scientific) was added and fluorescent readout made by Wallac 1420 Victor2 (Perkin Elmer). The resulting viability data was used to compute Combination Index scores as previously described (Schmidt et al., 2016). For further validation in a 3D tumor model over an extended time period, combinations of bortezomib with navitoclax or milciclib were selected for treatment of one bortezomib sensitive and one bortezomib resistant cell culture over 10 days.

Sphere growth combination treatments

For Figures 7F–7H, a total of 2000 cells from GBM cultures U3013MG and U3008MG were seeded in PrimeSurface 96U S-BIO plates (MoBiTech) in NSC medium with 2.5% matrigel basement membrane matrix (Corning). Following a short centrifugation step (30 s at 1000 rpm), cells were incubated for two days to allow sphere formation before adding treatments consisting of vehicle control, single drugs or combinations of bortezomib with navitoclax or milciclib diluted in DMSO. An initial dose-response screen with the single drugs and combinations in three-fold dilutions spanning a dose range from 1-100 nM (bortezomib), 0.11-1 μM (navitoclax) and 0.22-2 μM (milciclib) with two replicates per well was performed to select the most efficient combinations for a second phase experiment with seven replicate per treatment condition. In the second phase, two concentrations of bortezomib (3 and 10 nM) were combined with three different concentrations of navitoclax (1 μM, 0.33 μM and 0.11 μM) or milciclib (2 μM, 0.66 μM, 0.22 μM). Images were acquired with the Phase and Brightfield channels every 6 hours for an additional 10 days on the IncuCyte S3 instrument (Sartorius) using the spheroid scan module with the 4x objective. Brightfield channel images were segmented using the IncuCyte 2019B Rev2 software and the largest sphere area in each image was measured. Expected combination effects (white bar in Figures 7G and 7H) were computed using the Bliss model (below).

BrdU cell cycle flow cytometric analysis of bortezomib treated GBM cultures

For Figure S5, immunofluorescent staining of incorporated bromodeoxyuridine (BrdU) was performed using BrdU-FITC specific antibodies according to the manufacturerâ€s instructions (BD PharMingen, 559619) coupled with 7-amino-actinomycin (7-AAD) staining to permit cell cycle position analysis of cells with actively synthesizing DNA. Two proteasome inhibitor sensitive and two proteasome inhibitor-resistant GBM cultures were treated with DMSO vehicle, 10 or 50 nM bortezomib for 24 hours. During the final 1 hour of cultures, the cells were pulsed with 10 μM of BrdU before processing according to the BrdU Flow Kit protocol. Cell-associated BrdU levels and DNA content was measured on a CytoFLEX platform (Beckman Coulter) equipped with a 488-nm laser and analyzed using the CytExpert software version 2.4.

QUANTIFICATION AND STATISTICAL ANALYSIS

Algorithms for glioblastoma subtype assignment

Four methods for subtype assignment were combined by a weighted majority vote to designate one subtype for each primary GBM culture. Using the Verhaak (Verhaak et al., 2010) gene signature, NTP (Hoshida, 2010), ssGSEA (Barbie et al., 2009), k-NN (Xie et al., 2015), and nearest centroid were run using 1000 bootstrap runs resampling cell cultures. A majority vote over the 1000 runs gave the subtype vote for each classifier.

Drug target annotation

We annotated our drug library by Chemical Abstract Service (CAS) identifier, International Chemical Identifier (InChI) and STITCH database (CIDs/CIDm) identifiers. As a secondary source, we linked our library to the Drug Repurposing Hub. Target assignments were derived from the Drug Repurposing hub and STITCH. In the latter case, target assignments are gradual, and we used all targets with a score of at least 700/1000.

Algorithms for drug activity similarity and cluster analysis

From the 1544 compounds in Phase 1, 212 were selected based on their activity. Using drug targets annotated as described above, a randomization test (randomizing the drug-target annotations 10000 times) was run to derive an empirical p value for the frequency of targets selected among the 212 drugs. This resulted in 75 targets with an empirical p value of less than 0.05. The most highly enriched targets are shown in Figure 2A. Clustering of cell cultures and drugs was performed by compiling a matrix of mean viability across doses for each drug in each cell culture (cell cultures x compounds). To define subgroups of cell cultures, consensus clustering (Wilkerson and Hayes, 2010) using hierarchical clustering and Pearson distance metric was implemented using the ConsensusClusterPlus package in R Bioconductor. When clustering cell cultures, only the 80 compounds in the intersect between Phase 2 and Phase 3 was used. The optimal number of clusters was selected based on the diagnostic plots generated in the consensus clustering procedure (Figure S2A). To cluster drugs, a hierarchical clustering with Pearson distance metric and average linkage was used. The pairwise distances were computed omitting missing values. The final clusters were obtained using the *cutreeDynamicTree* function from the *dynamicTreeCut* package in R with the option *deepSplit* set to TRUE (Langfelder et al., 2008) and the minimum module size set to 5. For the heatmap in Figure 2, missing values were imputed using the *impute-knn* method in R, but the imputed values were not used in the clustering. A standard PCA solver (MATLAB) was used for PCA calculations (Figures 4A and 4B). In cases where more than one data type was used, all data were Z-transformed and stacked into a single matrix, before PCA.

Algorithms for construction of biomarker-drug network: drug response prediction based on multi-omic data

Prediction of drug response (quantified as the AUC score for each cell culture and drug) was performed using Random Forest (RF) (Breiman, 2001) and Elastic-Net (Zou and Hastie, 2005) methods implemented in R (*randomForest*, *glmnet*). Predictions were run for each drug separately (predicting one drug at a time), and using each datatype (mRNA expression, CNA, methylation, mutation) individually and in all unique combinations (e.g., CNA-methylation, methylation-mutation, methylation-mutation-CNA). For methylation data, the set of probes was reduced by removing probes methylated above an average value of 0.4 in reference brain using data from GEO series GSE41826 (Guintivano et al., 2013). Methylation was then summarized at the gene level by averaging the values of methylation probes in CpG islands within 1500 bases of the gene transcription start site. Gene level mutation data were filtered to include only genes with at least two mutated cases. Leave-one-out (LOO) cross-validation was used to assess the prediction performance by computing the Pearson correlation between the predicted and true values. Within each LOO-fold, internal cross-validation was used to select method parameters (e.g., lambda value for Elastic-Net). For each LOO-fold the variable importance was recorded (variable importance measure for RF and the absolute value of the Elastic-Net coefficient for Elastic-Net) and averaged over all LOO-folds for a particular drug. To construct the drug-variable network a variable was linked to a drug if the drug response was predicted with a Pearson correlation value above 0.2 and if that variable was among the top 50 most important variables for at least one prediction instance. The rather low threshold is used to encourage common predictors between drugs, and to allow for subsequent filtering of the network. To evaluate the impact of cross-validation method we compared 10-fold and leave-one-out CV using elastic net and expression data as the predictor. The 10-fold CV was averaged over 1000 runs. The prediction performance (CV-R) between the CV showed a Pearson correlation of 0.87. For each drug, a GSEA analysis (Subramanian et al., 2005) using the javaGSEA Jar file v 3.0 and MSigDB Hallmark gene sets (Liberzon et al., 2015), was performed using the gene expression data (filtered to the 10000 genes with highest standard deviation across cell cultures) with the drug response as a contious phenotype (1000 permutations of the phenotype with Pearson correlation metric). A drug is linked to an MSigDB pathway if the FDR q-value is less than 0.25. The links between drugs and MSigDB pathways were then added to the total network. For evaluating the difference between the cell cultures in Figure 3C, an anova p value was calculated comparing dose response curves of the two cell cultures using the package drc in R with a four-parameter Hill model.

Algorithms for scoring drug synergism

The effect on viability of each drug dose was calculated as a viability ratio W = (Ytreated-Yblank)/(Ycontrol-Yblank), where Ytreated represents the fluorescence signal in treated wells, Ycontrol the signal in vehicle-treated (DMSO) wells, and Yblank is the technical

background measured as the signal in cell-free (medium only) wells. Since drug pairs were analyzed across 6x6 pairwise combinations, we used a summary statistic defined as the minimum among the 6x6 epsilon values. Applied to the same data, we used the combination index, CI, defined as $CI(W) = (d_a(W)/D_a(W)) + (d_b(W)/D_b(W))$, where $D_a(W)$ and $D_b(W)$ are the single-agent dose of drugs a and b needed to reduce viability to level W, and $d_a(W)$, $d_b(W)$ are the doses of a and b needed to reduce viability to level W, when used as a combination. For the single dose data in the sphere experiments (Figures 7G and 7H), the simpler Bliss method was used, whereby the combination phenotype W_{ab} is compared to its naive expectation, defined by the product $W_a W_b$.